



1 **Ocean Acidification trends and Carbonate System dynamics in**
2 **the North Atlantic Subpolar Gyre during 2009-2019**

3 David Curbelo-Hernández¹, Fiz F. Pérez², Melchor González-Dávila^{1,*}, Sergey V.
4 Gladyshev³, Aridane G. González¹, David González-Santana¹, Antón Velo², Alexey Sokov³,
5 and J. Magdalena Santana-Casiano¹.

6 ¹ Instituto de Oceanografía y Cambio Global (IOCG), Universidad de Las Palmas de Gran
7 Canaria (ULPGC). Las Palmas de Gran Canaria, Spain.

8 ² Instituto de Investigaciones Marinas (IIM), CSIC, Vigo, Spain.

9 ³ P. P. Shirshov Institute of Oceanology, Russian Academy of Sciences, Moscow, Russian
10 Federation

11 *Corresponding Author: Melchor González-Dávila (melchor.gonzalez@ulpgc.es)

12 **Keypoints:**

13 During the 2010s, the subpolar North Atlantic experienced a 50-86% increase in
14 anthropogenic CO₂, accelerating by <10% the acidification.

15 Anthropogenic CO₂ contributed to acidification by 53-68% in upper layers and >82% in the
16 interior ocean.

17 The acidification trends (0.0006 and 0.0032 units yr⁻¹) declined the Ω_{Ca} and Ω_{Arag} by 0.004-
18 0.021 and 0.003-0.0013 units yr⁻¹, respectively.



19 **Abstract**

20 The CO₂-carbonate system dynamics in the North Atlantic Subpolar Gyre (NASPG) were
21 evaluated between 2009 and 2019. Data was collected aboard eight summer cruises through
22 the CLIVAR 59.5°N section. The Ocean Acidification (OA) patterns and the reduction in the
23 saturation state of calcite (Ω_{Ca}) and aragonite (Ω_{Arag}) in response to the increasing
24 anthropogenic CO₂ (C_{ant}) were assessed within the Irminger, Iceland and Rockall basins
25 during a poorly-assessed decade in which the physical patterns reversed in comparison with
26 previous well-known periods. The observed cooling, freshening and enhanced ventilation
27 increased the interannual rate of accumulation of C_{ant} in the interior ocean by 50-86% and
28 the OA rates by close to 10%. The OA trends were 0.0013-0.0032 units yr⁻¹ in the Irminger
29 and Iceland basin and 0.0006-0.0024 units yr⁻¹ in the Rockall Trough, causing a decline in
30 Ω_{Ca} and Ω_{Arag} of 0.004-0.021 and 0.003-0.0013 units yr⁻¹, respectively. The C_{ant} -driven rise
31 in total inorganic carbon (C_T) was the main driver of the OA (contributed by 53-68% in upper
32 layers and >82% toward the interior ocean) and the reduction in Ω_{Ca} and Ω_{Arag} (>64%). The
33 transient decrease in temperature, salinity and A_T collectively counteracts the C_T -driven
34 acidification by 45-85% in the upper layers and in the shallow Rockall Trough and by <10%
35 in the interior ocean. The present investigation reports the acceleration of the OA within the
36 NASPG and expands knowledge about the future state of the ocean.

37 **Keywords:** Ocean Acidification, Anthropogenic Carbon, North Atlantic Subpolar Gyre.



38 1. Introduction

39 The ocean uptake of approximately one-third of the CO₂ released into the atmosphere
40 (Friedlingstein et al., 2023; Gruber et al., 2019a) has an important role in the climate regulation
41 causing changes in the marine carbonate chemistry. The exponential increase in the global
42 ocean CO₂ sink in phase with those of anthropogenic emissions (Friedlingstein et al., 2023)
43 has resulted in a long-term decrease in the concentration of carbonate ions ([CO₃²⁻]) and pH.
44 This process has been collectively referred to as Ocean Acidification (OA; Caldeira and
45 Wickett, 2005, 2003; Doney et al., 2009; Orr et al., 2005; Raven et al., 2005; Feely et al., 2009)
46 and favour the dissolution of calcium carbonate (CaCO₃). It affects not only calcifying marine
47 organisms and ecosystems which use the biogenic CaCO₃ forms of calcite and aragonite (e. g.
48 Gattuso et al., 2015; Langdon et al., 2000; Pörtner et al., 2004, 2019; Riebesell et al., 2000)
49 but also the global biogeochemical cycles (Gehlen et al., 2011; Matear and Lenton, 2014).

50 The absorption of anthropogenic CO₂ has reduced the pH of the global surface ocean by 0.1
51 units since preindustrial times, representing approximately a 30% increase in acidity (Caldeira
52 and Wickett, 2003). The model projections estimate that the pH could fall by 0.5 units by the
53 end of the century if global CO₂ emissions continue to rise, while a drop of 0.2 units is expected
54 for the most conservative scenario (Caldeira and Wickett, 2005; Orr et al., 2005, 2011; Raven
55 et al., 2005). However, as the absorption and storing of anthropogenic carbon (C_{ant}) within the
56 ocean is not uniform (Sabine et al., 2004a), OA rates may show a significant spatial variability
57 and should be regionally studied. The temporal evolution of the carbonate system variables in
58 surface waters are monitored and assessed in several time-series stations located across
59 different ocean regions (Bates et al., 2014). The largest OA rates are expected to occur across
60 high northern and southern latitudes (Bellerby et al., 2005; Orr et al., 2005), where deep
61 convective overturning and subduction occur favouring the entrance of C_{ant} in the interior
62 ocean (Maier-Reimer and Hasselmann, 1987; Lazier et al., 2002; Sarmiento et al., 1992).

63 The North Atlantic is one of the strongest CO₂ sinks and stores over 25% of the C_{ant}
64 accumulated in the global ocean (e. g. Gruber et al., 2019; Khatiwala et al., 2013; Pérez et al.,
65 2024, 2010, 2008, 2024; Sabine et al., 2004; Takahashi et al., 2009). The Atlantic Meridional
66 Overturning Circulation (AMOC) plays a significant role by conveying acidified C_{ant} -loaded
67 waters polewards and exporting them to the ocean interior across deep-water formation areas



68 (Lazier et al., 2002; Pérez et al., 2013, 2008; Steinfeldt et al., 2009). It contributes to
69 homogenize the C_{ant} and pH in the whole water column in such regions and exported these
70 properties southwards to the global deep ocean (Perez et al., 2018). Thus, the North Atlantic
71 behaves as a crucial region for understanding the impacts of anthropogenic forcing on the
72 global ocean.

73 OA has been widely studied in the North Atlantic through the monitoring of the ocean
74 physicochemical properties at time-series stations (summarized by Bates et al., 2014) placed
75 in subtropical and subpolar latitudes: the European Station for Time series in the Ocean at the
76 Canary Islands (ESTOC; 29.04°N, 15.50°W; González-Dávila et al., 2010; González-Dávila
77 and Santana-Casiano, 2023; Santana-Casiano et al., 2007), the Bermuda Atlantic Time-series
78 Study (BATS; 32.0°N, 64.0°W; Bates et al., 2012), the Irminger Sea Time Series (IRM-TS;
79 64.3°N, 28.0°W; Olafsson et al., 2010) and the Iceland Sea Time Series (IS-TS; 68.0°N,
80 12.66°W; Olafsson et al., 2009, 2010). OA rates has also been evaluated along transects
81 through repeated hydrographic cruises (i.e. Guallart et al., 2015; García-Ibáñez et al., 2016;
82 Vázquez-Rodríguez et al., 2012b) or even covered by volunteer observing ships (Fröb et al.,
83 2019). These investigations have revealed a rate of decrease in pH of $\sim 0.001\text{-}0.002$ units yr^{-1} .
84 Moreover, González-Dávila and Santana-Casiano, (2023) has recently indicated that these
85 rates are increasing since 1995.

86 The assessment of OA is of especial interest across the North Atlantic Subpolar Gyre (NASPG;
87 50-60°N), where the atmospheric CO_2 sink is particularly strong and the deep-water formation
88 processes favour the storage of C_{ant} through the whole water column (Gruber et al., 2019b;
89 Sabine et al., 2004b; Watson et al., 2009, Pérez et al. 2008). Likewise, the deep-water
90 formation processes create the largest and deepest ocean environments supersaturated for
91 aragonite (at more than 2000 m depth; Feely et al., 2004; Jiang et al., 2015), which is the main
92 CaCO_3 mineral for Cold-water corals (CWC; Roberts et al., 2009) and some pteropods
93 (Bathmann et al., 1991; Urban-Rich et al., 2001). These deep biomes are predicted to be one
94 of the first in the global ocean affected by OA, mainly due to the shoaling of the Aragonite
95 Saturation Horizon and its progressive exposition to undersaturated conditions for aragonite at
96 intermediate and deep waters (Raven et al., 2005; Guinotte et al., 2006; Turley et al., 2007;
97 Roberts et al., 2009).



98 The physical processes along the NASPG, which are subject to significant spatiotemporal
99 variability introduced by the atmospheric forcing and climatology on an interannual scale,
100 directly influenced the biogeochemistry (Corbière et al., 2007; Fröb et al., 2019). The changes
101 in North Atlantic Current (NAC) modifies the poleward heat transport from subtropical
102 latitudes and the air-sea interactions, influencing temperature patterns (Josey et al., 2018;
103 Mercier et al., 2015). Recent studies noticed the surface cooling and freshening of the NASPG
104 in the 2010s (Holliday et al., 2020; Josey et al., 2018; Robson et al., 2016; Tesdal et al., 2018)
105 contrasting with the period of warming and salinification in the 1990s extended until 2005
106 (Häkkinen and Rhines, 2004; Hátún et al., 2005; Robson et al., 2014). Anomalously heat loss
107 and winter deep convection were found to be of high intense since 2008 contributing to the
108 extreme cold anomaly along the NASPG (e. g. De Jong et al., 2012; de Jong and de Steur,
109 2016; Fröb et al., 2019, 2016; Gladyshev et al., 2016b, 2016a; Piron et al., 2017; Våge et al.,
110 2009). These fluctuations in the vertical mixing and ocean circulation patterns introduces
111 changes in the distribution of the carbonate system variables.

112 Several investigations have evaluated the drivers, trends and impacts of OA in the western
113 NASPG at the Irminger and Iceland basins (e. g. Fontela et al., 2020; García-Ibáñez et al.,
114 2021, 2016; Perez et al., 2018; Pérez et al., 2021; Ríos et al., 2015), while few studies have
115 addressed it along the Rockall Trough (e. g. McGrath et al., 2013, 2012a, 2012b, Humphreys
116 et al., 2016) due to lack of repeated hydrographic sections or time-series stations and
117 subsequent limitation of continuous surface-to-bottom data. The high longitudinal variability
118 in the NASPG caused by the influence of different circulation patterns and water masses
119 (García-Ibáñez et al., 2018, 2015) introduced several physicochemical heterogeneities
120 between the Irminger and Iceland with the Rockall basin (Ellett et al., 1986; McGrath et al.,
121 2013, 2012b; Holliday et al., 2000). These differences in the distributions of Marine Carbonate
122 System (MCS) variables should be considered to improve our understanding of OA in the
123 entire North Atlantic.

124 This study evaluated the OA in the NASPG across the Irminger, Iceland and Rockall basins
125 during the 2010s. High-quality direct measurements of CO₂ system variables from eight
126 hydrographic cruises occupying 59.5°N between 2009 and 2019 were used to evaluate the
127 drivers and trends of pH, and the potential effects of OA on calcifying organisms of changes



128 in calcite (Ω_{Ca}) and aragonite (Ω_{Ar}) saturation states. This study advances our understanding
129 of the complexities associated with OA in the NASPG and supports ongoing efforts to model
130 and predict future acidification scenarios in the North Atlantic and global ocean.

131 **2. Methodology**

132 **2.1. Data collection**

133 Data was collected along the hydrographic CLIVAR 59.5°N section (Daniault et al., 2016;
134 Gladyshev et al., 2016c, 2018, 2017; Sarafanov et al., 2018) from 8 summer cruises with dates
135 spanning 11 years (2009-2019). The section covers the length of the North Atlantic at 59.5°N
136 between Scotland and Greenland (4.5-43.0°W), crossing the Irminger and Iceland basins and
137 the Rockall Trough (Figure 1). Generally, the sampling stations were equidistantly spaced
138 every 20 nmi apart ($\sim 1/3^\circ$ longitude) and repeated in all the cruises except for the cruise of
139 2016, when the station spacing was decreased to 10 nmi over Reykjanes Ridge western and
140 eastern slopes. The distance between stations over the east Greenland slope and shelf always
141 decreased from 10 nmi to about 2 nmi. The surface-to-bottom sampling and in situ
142 measurements were performed by using a SBE 911plus CTD with SBE32 Carousel containing
143 24 Niskin bottles (10 L) with additional sensors for pressure (P), dual temperature (T) and
144 salinity (S), and dissolved oxygen (DO). The eight cruises included in the new dataset are the
145 result of an international collaboration between researchers from the P. P. Shirshov Institute of
146 Oceanology at the Russian Academy of Science and the Marine Chemistry research group
147 from the Oceanography and Global Change Institute (QUIMA-IOCAG) at the University of
148 Las Palmas de Gran Canaria (ULPGC). A detailed overview and metadata of the cruises is
149 given in Table 1.

150 **2.1.1. CO₂ system variables measurements**

151 The analysis of the MCS variables followed the same analytical methodology and provided
152 high-quality CO₂ measurements in all the hydrographic cruises. It includes the sampling and
153 data collection techniques, quality control and calculation procedures published in the updated
154 version of the DOE method manual for CO₂ analysis in seawater given by Dickson et al., 2007.
155 The seawater samples were onboard analysed for total alkalinity (A_T) and total inorganic
156 carbon (C_T) determination by using a VINDTA 3C and following Mintrop et al., (2000). The
157 A_T was analysed by potentiometric titration with HCl to the carbonic acid endpoint and



158 determined through the developing of the full titration curve (Millero et al., 1993; Dickson and
159 Goyet, 1994). The C_T was determined through coulometric titration (Johnson et al., 1993). The
160 VINDTA 3C was *in situ* calibrated through the titration of Certified Reference Material
161 (CRMs; provided by A. Dickson at Scripps Institution of Oceanography), giving values with
162 an accuracy of $\pm 1.5 \mu\text{mol kg}^{-1}$ for A_T and $\pm 1.0 \mu\text{mol kg}^{-1}$ for C_T .

163 Spectrophotometric pH measurements (Clayton and Byrne, 1993) in total scale at constant
164 temperature of 15°C ($\text{pH}_{T,15}$) were performed for the cruises between 2009 and 2016. A
165 spectrophotometric pH sensor (SP101-SM) developed by the QUIMA-IOCAG group at the
166 ULPGC in collaboration with SensorLab (González-Dávila, 2014; González-Dávila et al.,
167 2016) was used. The method uses 4 wavelengths analysis for the m-cresol purple, includes
168 auto-cleaning steps and performs a blank for pH calculation immediately after the dye
169 injection. The spectrophotometric sensor was *in situ* tested by using a TRIS seawater buffer
170 and provided $\text{pH}_{T,15}$ values with an accuracy of ± 0.002 units. However, DelValls and Dickson,
171 (1998) reported an uncertainty of the spectrophotometric pH determination associated to the
172 TRIS used for calibration of -0.0047 units. Hence, the experimental pH values were corrected
173 by adding 0.0047 units.

174 **2.1.2. Dissolved oxygen (DO) measurements**

175 The WINKLER method introduced by Winkler (1888) and optimized by Carpenter (1965) and
176 Carrit and Carpenter (1966) was used to analytically determine the dissolved oxygen (DO) of
177 the seawater samples in all the cruises from 2009 to 2016. The seawater samples for DO
178 determination were collected from the bottle samples in pre-calibrated glass wide-neck bottles
179 avoiding bubble formation. The temperature of the water was recorded during the sampling.
180 All the reagents and solutions used for dissolved oxygen determination were prepared
181 following the procedures described by Dickson and Goyet (1994) and their possible impurities
182 were controlled by determining a blank every 2 days.

183 As DO could not be analytically measured during the cruise of 2019 (due to limitations
184 related with the oceanographic cruise plan), it was computed for this year by comparing the
185 performance of the DO sensor during the cruise of 2019 versus (1) DO data estimated by a
186 neural network for the cruises of 2016 and 2019 and (2) WINKLER-measured DO data in
187 the cruise of 2016. The neural network ESPER_NN (Empirical Seawater Property Estimation



188 Routine) introduced by Carter et al., (2021) was used for DO estimations. The computational
189 procedure is detailed in Appendix A.

190 **2.2. Data processing**

191 **2.2.1. Evaluation of the internal consistency of the data using CANYON-B**

192 The measured and determined data were compared with estimations given by the Bayesian
193 neural network “CANYON-B” (Bittig et al., 2018), a re-developed and more robust neural
194 network based on CANYON (CARbonate system and Nutrients concentration from
195 hYdrological properties and Oxygen using a Neural-network; Sauzède et al., 2017).
196 CANYON-B estimates the four MCS variables (A_T , C_T , pH_T and pCO_2) and macronutrients
197 concentrations (PO_4^{3-} , NO_3^- and $Si(OH)_4$, hereinafter PO_4 , NO_3 and $Si(OH)_4$) as a function of
198 a simple set of input variables which include P, T, S, DO, latitude, longitude and date. This
199 neural network is trained on and validated against bottle and sensor data from GLODAPv2,
200 GO-SHIP and Argo profiles, and provides a local uncertainty for each variable. The standard
201 errors of estimate reported for CANYON-B by Bittig et al., (2018) are $6.3 \mu\text{mol kg}^{-1}$ for A_T ,
202 $7.1 \mu\text{mol kg}^{-1}$ for C_T , 0.013 units for pH, $20 \mu\text{atm}$ for pCO_2 , $0.051 \mu\text{mol kg}^{-1}$ for PO_4 , 0.68
203 $\mu\text{mol kg}^{-1}$ for NO_3 and $2.3 \mu\text{mol kg}^{-1}$ for $Si(OH)_4$. The crossover analysis between measured
204 and estimated data did not show systematic differences but individual outliers. The measured
205 data that were higher/lower than the CANYON-B estimate by plus/minus twice the predicted
206 variable uncertainty of the neural network were considered as outliers and removed from the
207 dataset.

208 The total amount of measured data was 8974 for A_T , 7495 for C_T , 8706 for pH_T , 9656 for DO,
209 9114 for PO_4 and 9192 for $Si(OH)_4$. The difference between the measured and CANYON-B-
210 estimated variables (referred hereinafter as canyon-estimated variables) were performed for
211 each sample in which CANYON-B could be applied (samples with availability of T, S and DO
212 measurements). The number of data, mean values and standard deviation of the measured
213 variables for each cruise were summarized in Table S1. The average differences with the 95%
214 confidence interval for each cruise are shown in Table S2. The average differences for the
215 entire period (2009-2019) were lower than $2.1 \mu\text{mol kg}^{-1}$ for A_T , $2 \mu\text{mol kg}^{-1}$ for C_T , 0.0002 for
216 pH_T , $0.02 \mu\text{mol kg}^{-1}$ for PO_4 and $0.25 \mu\text{mol kg}^{-1}$ for $Si(OH)_4$.

217 **2.2.2. Computational methods**



218 The computational procedures to calculate MCS system variables applied in this investigation
219 used the CO₂SYS programme developed by Lewis and Wallace, (1998) and run with the
220 MATLAB software (van Heuven et al., 2011; Orr et al., 2018; Sharp et al., 2023). The set of
221 constants used for computations includes the carbonic acid dissociation constants of Lueker et
222 al., (2000), the HSO₄⁻ dissociation constant of Dickson, (1990), the HF dissociation constant
223 of Perez and Fraga, (1987) and the value of [B]_T determined by Lee et al., (2010). The pH in
224 total scale at *in situ* temperature (pH_T) was computed from the measured A_T and pH_{T,15} (the
225 computed C_T was given as an output). The pH_T for the cruise of 2019, in which direct pH
226 measurements were not performed, was computed from the measured A_T and C_T .

227 In addition, as three of the four MCS variables were measured in the rest of the cruises and
228 due to gaps in data, an intercomparison between measured and computed C_T and pH_{T,15} was
229 performed. It considers the availability of measurements for each latitude, longitude and time
230 and the differences between the measured and computed pH with the canyon-estimated pH_T.
231 The use of measured or computed C_T followed these conditions: (1) If there is measured C_T
232 but not measured pH, measured C_T was used, (2) if there is measured pH but not measured C_T ,
233 computed C_T was used, (3) and if there is measured C_T and pH, measured C_T was used when
234 the differences between measured and canyon pH_T is lower than the differences between
235 computed and canyon-estimated pH_T, while computed C_T was used when the opposite
236 happens. In total, 6375 measured and 2872 computed C_T data were used in this study (69%
237 and 31%, respectively). The average differences in each cruise between the combined
238 (measured and computed, also referred as " $C_{T(new)}$ ") and canyon-estimated C_T variable is
239 provided in Table S2. The amount and percentage of measured and computed C_T data per
240 cruise is given in Table S3. As the measured C_T was in average 1.9 $\mu\text{mol kg}^{-1}$ higher than the
241 canyon-estimated and the computed C_T was in average 1.7 $\mu\text{mol kg}^{-1}$ lower, the new
242 compilation based on these previous conditions allowed to reduce the difference to 1.5 μmol
243 kg^{-1} .

244 2.2.3. Anthropogenic CO₂ (C_{ant}) calculation

245 The anthropogenic CO₂ (C_{ant}) was estimated by using the biogeochemical back-calculation
246 ϕC_T° method, which has an overall estimated uncertainty of $\pm 5.2 \mu\text{mol kg}^{-1}$ (Pérez et al., 2008;
247 Vázquez-Rodríguez et al., 2009). The method considers the change of C_T between the



248 preindustrial era (1750) and the time of the observations, as well as the processes involved in
249 the uptake and distribution of C_{ant} (biogeochemistry, mixing processes and air-sea fluxes). The
250 C_{ant} was calculated (Eq. 1) as the difference between the C_T at the time of observation, the C_T
251 that the seawater would have in equilibrium with a preindustrial atmosphere (preformed C_T ;
252 C_T^{pre}), the offsets of such equilibrium values (air-sea CO_2 disequilibrium; ΔC_T^{dis}) and the
253 changes in C_T due to the organic and carbonate pumps (ΔC_T^{bio}). The C_T and A_T at the time of
254 observations and the preformed A_T (A_T^0) are needed as input parameters and the computational
255 procedure was described by Vázquez-Rodríguez et al., (2012).

$$256 \quad C_{ant} = C_T - C_T^{pre} - \Delta C_T^{dis} - \Delta C_T^{bio} \quad (1)$$

257 The ϕC_T^0 method is an improved process-based C_{ant} estimation method tested and widely
258 applied in the Atlantic Ocean (Vázquez-Rodríguez et al., 2009) which present distinctive
259 characteristics relative to existing C_{ant} approaches, such as the classical ΔC^* (GSS' 96; Gruber
260 et al., 1996) and the TrOCA (Touratier et al., 2007). The main advantages of the ϕC_T^0 method
261 has been described by Pérez et al., (2008).

262 **2.2.4. Water mass characterization**

263 The characterization of the basins and water masses was done by considering the 2006-2021
264 mean combined CLIVAR 59.5°N section constructed with potential vorticity, dissolved oxygen
265 and salinity together with the large-scale circulation in the North Atlantic (e. g. Lherminier et
266 al., 2010; Pérez et al., 2021; Sarafanov et al., 2012; Schmitz and McCartney, 1993; Schott and
267 Brandt, 2007; Sutherland and Pickart, 2008). A schematic diagram with the main surface and
268 deep currents in the NASPG is depicted in Figure 1a. The basin division considered the NAC
269 pathways and revealed a west-to-east distribution comprising the Irminger and Iceland basins
270 and the Rockall Trough. The Iceland basin was delimited along its eastern boundary by the
271 central NAC branches around the northern part of the Haton Bank and George Bligh Bank,
272 and along its western boundary by the Return Current over the eastern flank of the Reykjanes
273 Ridge slope. This suggest that the Iceland basin could be longitudinally separated in two
274 subregions: the western Iceland basin (24.0-29.5°W) and the eastern Iceland basin (14.0-
275 24.0°W).



276 The upper layers were mainly occupied by Subpolar Mode Waters (SPMW) and North Atlantic
277 Central Waters (NACW). SPMW is formed in the Iceland basin (McCartney and Talley, 1982;
278 Brambilla and Talley, 2008; Tsuchiya et al., 1992; Van Aken and Becker, 1996), flow eastward
279 to the Rockall Trough and recirculate across the Reykjanes Ridge (Brambilla and Talley, 2008).
280 In the Irminger basin, SPMW flow with the Irminger Current to the north over the western
281 Reykjanes Ridge flank and to the south over the eastern Greenland slope (Figure 1a). Thus,
282 SPMW signal was detected in the western and eastern Irminger basin up to 400-700 m depth
283 and limited to subsurface depths in the central part of the basin. NACW were placed above
284 SPMW east of the Irminger basin and separated in two branches: Eastern North Atlantic
285 Central Water (ENACW), formed by winter convection in the intergyre region and moved
286 poleward from the Bay of Biscay through the Rockall Trough (Harvey, 1982; Pollard et al.,
287 1996), and Western North Atlantic Central Water (WNACW), flowing northward with the
288 NAC along the western Iceland basin. The intermediate layers were mainly occupied by
289 Labrador Sea Water (LSW), formed in the Labrador Sea and transported eastward (e. g. Pickart
290 et al., 2003; Fröb et al., 2016). LSW path diverges into two cores when it reaches the Reykjanes
291 Ridge (Álvarez et al., 2004; Pickart et al., 2003): a fraction of LSW rapidly moved to the
292 Irminger basin and incorporated into the Deep Western Boundary Current (DWBC) (Bersch et
293 al., 2007) and a second LSW core was transported eastward into the Iceland and Rockall
294 basins. In the Irminger and western Iceland basin, LSW placed above Iceland-Scotland
295 Overflow Water (ISOW), which originated from the overflow of Norwegian Sea waters over
296 the Iceland–Scotland ridges and flowed southward and below 1500 m depth through the
297 western NASPG (van Aken and de Boer, 1995; Dickson et al., 2002; Fogelqvist et al., 2003).
298 The bottom of the western Irminger basin was occupied by Denmark Strait Overflow Water
299 (DSOW), recently formed from deep waters from the Nordic seas flowing southward over the
300 Greenland-Iceland ridge and sinking through the eastern Greenland slope (Read, 2000;
301 Stramma et al., 2004; Yashayaev and Dickson, 2008). LSW core transported eastwards rises
302 in depth through the western Haton Bank flank and occupy the bottom depths in the eastern
303 Iceland basin and in the Rockall Trough. A low-ventilated thermocline layer is placed between
304 SPMW and LSW in the eastern NASPG (García-Ibáñez et al., 2016), which represent the
305 product of mixing with waters coming from the south (i. e. Mediterranean Waters; MW).



306 The physical and biogeochemical interannual changes were analysed in the main basins and
307 water masses. In order to enhance the comprehension of the spatial distribution and trends of
308 the biogeochemical variables and to facilitate comparisons with previous studies along the
309 NASPG, the hydrographic characterization was simplified based on the following principles:
310 (1) the Iceland basin was not divided into its western and eastern parts and its longitudinal
311 span was delimited by the Reykjanes Ridge (29.5°W) and the Haton Bank (17°W), (2) upper
312 Labrador Sea Water (uLSW) was separated from deeper LSW (e. g. Stramma et al., 2004), (3)
313 the weak and spatially-limited influence of the return current and WNACW was removed by
314 considering the upper and intermediate layers of both the Irminger and Iceland basin fully
315 occupied by SPMW above uLSW, and (4) only the east branch of NACW (ENACW), placed
316 above SPMW, was contemplated for the upper Rockall Trough.

317 The whole water column was separated in layers delimited by potential density isopycnals at
318 a reference pressure of 0 dbar following Azetsu-Scott et al. (2003), Kieke et al. (2007), Pérez
319 et al. (2008) and Yashayaev et al. (2008). The vertically distributed water masses separated in
320 density layers is represented for the entire section in Figure 1b. The vertical characterization
321 in density layers allows to consistently compare the low-variable physical and chemical
322 properties within each water mass, enabling to assume linearity in the ocean CO₂ system. The
323 determination of the isopycnal limits between layers in the Irminger and Iceland basins
324 followed previous biogeochemical studies in the western boundary of the North Atlantic
325 (Fontela et al., 2020; García-Ibáñez et al., 2016; Pérez et al., 2010, 2008; Vázquez-Rodríguez
326 et al., 2012a). The surface-to-bottom distribution of the main water masses in these basins
327 (with their respective σ_0 lower limits shown in brackets) was SPMW (27.68 kg m⁻³), uLSW
328 (27.76 kg m⁻³), LSW (27.81 kg m⁻³) and ISOW (27.88 kg m⁻³). The low temperature and
329 salinity DSOW were considered at the bottom of the westernmost part of the Irminger basin.
330 The hydrography of the Rockall Trough has been characterized in previous studies in the
331 Northeast Atlantic (e. g. Ellett et al., 1986; Harvey, 1982; McGrath et al., 2012a, 2012b;
332 Holliday et al., 2000). The considered surface-to-bottom distribution of the main water masses
333 was ENACW (27.35 kg m⁻³), SPMW (27.68 kg m⁻³) and LSW (bottom).

334 **2.2.5. pH_T trends deconvolution**



335 OA trends arise due to the combined variations in T, S, C_T and A_T . The influence of each driver
 336 on OA was analysed by assuming linearity and employing a first-order Taylor-series
 337 deconvolution to evaluate the pH_T trends (Fröb et al., 2019; García-Ibáñez et al., 2016; Pérez
 338 et al., 2021; Takahashi et al., 1993; Tjiputra et al., 2014). Partial derivatives of pH_T versus T,
 339 S, C_T and A_T were calculated based on mean properties of each layer by using the most recent
 340 equation (Eq. 2) given by Pérez et al., (2021). This equation introduced salinity-normalized C_T
 341 and A_T ($NX_T = X_T/S*35$) to remove the effect of the freshwater fluxes in the variation of A_T
 342 and C_T .

$$343 \quad \frac{dpH_T}{dt} = \frac{\partial pH_T}{\partial T} \frac{dT}{dt} + \left(\frac{\partial pH_T}{\partial S} + \frac{NC_T}{S_0} \frac{\partial pH_T}{\partial C_T} + \frac{NA_T}{S_0} \frac{\partial pH_T}{\partial A_T} \right) \frac{dS}{dt} + \frac{S}{S_0} \frac{\partial pH_T}{\partial C_T} \frac{dNC_T}{dt} + \frac{S}{S_0} \frac{\partial pH_T}{\partial A_T} \frac{dNA_T}{dt} \quad (2)$$

344 It is important to remark that the changes in NA_T and NC_T are linked with biogeochemical
 345 processes which have different influences: the processes involved in the organic carbon pump
 346 contribute to strongly change the NC_T weakly affecting the NA_T , while those involved in the
 347 carbonate pump affect the NA_T twice as much as NC_T . The complexity and heterogeneity of
 348 the processes that govern the pH_T change were considered by this equation.

349 **2.2.6. Calculation of the state of saturation of Calcite (Ω_{Ca}) and Aragonite (Ω_{Arag}):** 350 **trends and drivers**

351 The adverse impacts of OA on marine calcification processes and its correlation with the
 352 saturation states of Calcite (Ω_{Ca}) and Aragonite (Ω_{Arag}) has been commonly demonstrated (e.
 353 g. Gattuso et al., 2015; Langdon et al., 2000; Pörtner et al., 2004, 2019; Riebesell et al., 2000).
 354 The Ω_{Ca} and Ω_{Arag} were calculated as the product of the ion concentrations of calcium ($[Ca^{2+}]$)
 355 and carbonate ($[CO_3^{2-}]$) divided by the stoichiometry solubility products (K_{sp}) for calcite (K_{Ca})
 356 and aragonite (K_{Arag}) given by Mucci (1983) (Eq. 3 and 4). The Ω_{Ca} and Ω_{Arag} were calculated
 357 with the CO2SYS programme (Lewis and Wallace, 1998) for MATLAB (van Heuven et al.,
 358 2011; Orr et al., 2018; Sharp et al., 2023), applying the set of constants detailed in section
 359 2.2.2.

$$360 \quad \Omega_{Ca} = \frac{[Ca^{2+}][CO_3^{2-}]}{K_{Ca}} \quad (3)$$

$$361 \quad \Omega_{Arag} = \frac{[Ca^{2+}][CO_3^{2-}]}{K_{Arag}} \quad (4)$$



362 The collective temporal changes in the physico-chemical properties governing the OA
363 influenced the \mathcal{Q}_{Ca} and \mathcal{Q}_{Arag} variations and were considered in this study. The influence of the
364 potential drivers was analysed by employing a first-order Taylor-series deconvolution to
365 evaluate the \mathcal{Q}_{Ca} and \mathcal{Q}_{Arag} trends, as done with the pH_T (section 2.2.5). Likewise, the
366 interannual changes of \mathcal{Q}_{Ca} and \mathcal{Q}_{Arag} were assumed linear and given by the sum of the partial
367 derivatives of \mathcal{Q}_{Ca} and \mathcal{Q}_{Arag} versus each driver (García-Ibáñez et al., 2021) in Eq. 5.

$$368 \quad \frac{d\Omega}{dt} = \frac{\partial\Omega}{\partial T} \frac{dT}{dt} + \left(\frac{\partial\Omega}{\partial S} + \frac{NC_T}{S_0} \frac{\partial\Omega}{\partial C_T} + \frac{NA_T}{S_0} \frac{\partial\Omega}{\partial A_T} \right) \frac{dS}{dt} + \frac{S}{S_0} \frac{\partial\Omega}{\partial C_T} \frac{dNC_T}{dt} + \frac{S}{S_0} \frac{\partial\Omega}{\partial A_T} \frac{dNA_T}{dt} \quad (5)$$

369 **3. Results**

370 **3.1. Physicochemical characterization of the water column**

371 The vertical distribution of the physical and biogeochemical variables is depicted in Figures 2,
372 3, S2 and S3. These figures exhibited the changes in the water-column properties throughout
373 the section between 2009 and 2016. The subsurface layers were characterized by warmer and
374 saltier waters than intermediate and deep layers among the three basins (Figure 2a and 2b). A
375 West-to-East increase in temperature and salinity throughout the water column was observed
376 in all the cruises. The temperature and salinity signals were highest in the Rockall Trough (4.5-
377 11.0°C and 35.0-35.4, respectively), followed by the Iceland basin (3.0-7.5°C and 34.9-35.2,
378 respectively) and the Irminger basin (1.5-6.5°C and 34.8-35.1, respectively). The longitudinal
379 differences in temperature were more remarkable toward the upper layers through the SPMW
380 and uLSW.

381 The spatial variability in the physical properties introduced heterogeneities in the distribution
382 of the CO₂ system variables. The A_T show a well-correlated direct relationship with salinity
383 throughout the section ($r^2=0.89$), with lower and vertically-homogenized average values in the
384 Irminger basin (2302.8-2307.3 $\mu\text{mol kg}^{-1}$ in subsurface waters and 2298.8-2301.0 $\mu\text{mol kg}^{-1}$
385 in bottom waters) and Iceland basin (2308.7-2315.0 $\mu\text{mol kg}^{-1}$ in subsurface waters and
386 2305.2-2308.0 $\mu\text{mol kg}^{-1}$ in bottom waters) compared to the Rockall Trough (2317.9-2329.1
387 $\mu\text{mol kg}^{-1}$ in subsurface waters and 2308.5-2310.9 $\mu\text{mol kg}^{-1}$ in bottom waters). The upper
388 layers were characterized by low C_T values (2153.7-2160.8 $\mu\text{mol kg}^{-1}$ at the Irminger basin,
389 2158.1-2168.4 $\mu\text{mol kg}^{-1}$ at the Iceland basin and 2120.1-2131.0 $\mu\text{mol kg}^{-1}$ at the Rockall
390 Trough), while a rapidly increment with depth was found below 100-200 m depth (2154.7-



391 2171.2 $\mu\text{mol kg}^{-1}$ throughout the section). The notable difference in the distribution of A_T and
392 C_T (Figure 2c and 3a, respectively) compared to those of NA_T and NC_T (Figure S2) elucidated
393 the remarkable significance of freshwater fluxes on the carbon variables fluctuations during
394 the period of study. The entrance of C_{ant} through the atmosphere-seawater interface caused
395 higher C_{ant} values in the upper layers (higher than 50 $\mu\text{mol kg}^{-1}$ in the first 1000 m depth;
396 Figure 3b). The natural component of the C_T ($C_{\text{nat}}=C_T-C_{\text{ant}}$; Figure 3c) correlated with C_T
397 ($r^2=0.87$), and show a distribution characterized by low surface ($<2110 \mu\text{mol kg}^{-1}$) and high
398 bottom concentrations ($>2130 \mu\text{mol kg}^{-1}$).

399 The pH_T (Figure 2d) rapidly decreased with depth showing the effect of biological uptake in
400 the upper layers and remineralization in deeper areas. The subsurface layer up to 100-200 m
401 depth exhibited pH_T values higher than 8.025 units, which fell to 7.975 units at the bottom
402 layers. The pH_T profiles reported an intrusion of remineralized and poorly oxygenated water
403 between 500 and 1000 m depth with relatively low pH_T (<7.975) compared to adjacent layers
404 in the Iceland basin and in the western part of the Rockall Trough. This thermocline layer was
405 previously observed at ~ 500 m depth by García-Ibáñez et al., (2016) along a more meridional
406 transect which crossed the Iceland basin northwest-southeast. It introduces differences in the
407 intermediate water masses between the Iceland and Rockall basins with the Irminger basin.

408 The spatial and interannual fluctuations in the ventilation rates through changes in the water
409 mass formation and respiration processes represent a source of variability in the
410 biogeochemical patterns. The apparent oxygen utilization (AOU), defined as the difference
411 between saturated oxygen (calculated following Benson and Krause, 1984) and measured
412 oxygen, was used to assess the ventilation of the water masses (Figure 2e). The high AOU
413 values indicate low ventilation, while low AOU values indicate the opposite. The slow renewal
414 of waters with high AOU favour the accumulation of the product of remineralization (de la
415 Paz et al. 2017). Thus, the areas with higher AOU (Figure 2e) were found to have high
416 concentration of C_T and low pH_T (Figures 3a and 2d, respectively). The near surface waters
417 permanently in contact with the atmosphere exhibited the lowest AOU values ($<20 \mu\text{mol kg}^{-1}$).
418 The Irminger Basin presents the most significant water column ventilation among the entire
419 section, with maximum AOU ranging from 35 to 50 $\mu\text{mol kg}^{-1}$ at the LSW and ISOW and the
420 remarkable intrusion of oxygenated DSOW ($>260 \mu\text{mol kg}^{-1}$ DO) over the continental slope



421 with AOU ranging from 30 to 40 $\mu\text{mol kg}^{-1}$. The intermediate and deep layers of the Iceland
422 and Rockall basins were less ventilated, with AOU values higher than 45-50 $\mu\text{mol kg}^{-1}$. The
423 thermocline layer placed between 500 and 1000 m depth along these two basins presented the
424 highest maximum AOU throughout the period ($>60 \mu\text{mol kg}^{-1}$). The stagnation of these waters
425 corresponds with the high C_T and low pH_T (Figures 3a and 2d, respectively) encountered at
426 intermediate depths and should be considered in its temporal evolution.

427 **3.2. Temporal evolution of the physicochemical properties**

428 The interannual trend in the distribution of the physicochemical properties was analysed
429 through the whole water column across the Irminger, Iceland and Rockall basins by yearly
430 averaging the variables for each layer, following previous studies in the NASPG (e.g. Fontela
431 et al., 2020; García-Ibáñez et al., 2016) and applying linear regressions, where the ratios of
432 interannual change were given by the values of the slopes. The temporal distribution and trends
433 of the average physicochemical properties (Figures 4, 5, 6, S4, S5 and S6) revealed remarkable
434 heterogeneities in their interannual evolution within the period 2009-2019 among the different
435 basins and water masses. The mean properties were represented with error bars that are two
436 times the error of the mean ($2\sigma = 2 * (\text{Standard Deviation}/\sqrt{n})$, where n is the number of
437 bottle samples in each layer and cruise. The interannual ratios are presented along with their
438 respective standard error of estimate and correlation factors (r^2 and p-value) in Table 3 and S4.
439 The standard errors of the slopes were calculated by considering the standard error of the
440 annual mean values. The p-values ≤ 0.01 indicated that the trends were statistically significant
441 at the 99% confidence level, the p-values ≤ 0.05 indicated that the trends were statistically
442 significant at the 95% confidence level and the p-values ≤ 0.1 indicated that the trends were
443 statistically significant at the 90% level. Trends with p-values > 0.1 were considered as not
444 statistically significant but provided an estimation of the temporal evolution of the variables
445 in their respective layers. These not statistically significant trends were explained by the high
446 variability and changes in the low-limit depth of the layers encountered between consecutive
447 years.

448 As there was a lack of in situ measurements and sampling along the west half of the Irminger
449 basin (36.5-42.5°W) in the cruise of 2019 (due to permit restrictions to study the national
450 waters of Denmark), the GO-SHIP A25-OVIDE data for the cruise of 2018 (available at



451 SEANOE [<https://www.seanoe.org/>], Pascale et al., 2022) were considered to adjust the 2019
452 data. The average values were calculated with both the available data in the easternmost part
453 of the Irminger basin during the cruise of 2019 and the A25-OVIDE-2018 data available in
454 the same part of the section (29.6-36.5°W). The difference between these average values
455 provides the variation of each variable from 2018 to 2019, which can be extrapolated to the
456 western part of the Irminger basin by assuming linearity in the temporal evolution. Thus, the
457 average values for 2019 were adjusted by applying the product with the calculated change
458 between 2018 and 2019.

459 **4. Discussion**

460 **4.1. Reversal of the physical trends during the 2010s**

461 The present investigation revealed the cooling and freshening of the upper ocean in the
462 NASPG within the period 2009-2019 (Figure 4; Table 2), as recently reported since the reversal
463 of climatic trend and surface physical properties occurring after 2005 (Holliday et al., 2020;
464 Josey et al., 2018; Robson et al., 2016; Tesdal et al., 2018). The temperature decreased in the
465 upper ocean (with more than 95% level of confidence in SPMW, while non statistically
466 significant in ENACW) by 0.05-0.08 °C yr⁻¹ (Table 2), which is consistent with the ratio of
467 heat loss per decade among the first 700 m depth equivalent to approximately -0.45 °C decade⁻¹
468 (-0.045 °C yr⁻¹) encountered over the period 2005-2014 (Robson et al., 2016). The interannual
469 temperature trends in subsurface layers (Table 2) similarly draw the cooling observed in the
470 Irminger basin between 2008 and 2017 (-0.05 and -0.11 °C yr⁻¹ for summer and winter,
471 respectively; Leseurre et al., 2020) and the winter average surface cooling along the entire
472 NASPG between 2004 and 2017 (-0.08 ± 0.02 °C yr⁻¹; Fröb et al., 2019). The decrement in
473 subsurface salinity (with more than 95% level of confidence in both SPMW and ENACW) of
474 0.006-0.018 yr⁻¹ (Table 2) agreed with the interannual rates provided by Tesdal et al., (2018)
475 for the Irminger basin (-0.007 ± 0.002 yr⁻¹) and for the central-eastern NASPG (-0.020 ± 0.003
476 yr⁻¹) over the period 2004-2015.

477 The fluctuations in physical properties were linked to a decrease in oceanic heat transport and
478 storage within the NASPG, which has been attributed to changes in the AMOC over decadal
479 to multidecadal timescales (Balmaseda et al., 2007; Desbruyères et al., 2013; Mercier et al.,
480 2015; Smeed et al., 2018). However, the assessment of the temporal evolution of the AMOC



481 in high latitudes remains uncertain, and there is no evidence of its impact on physical patterns
482 across the NASPG on an interannual scale (Jackson et al., 2022). The changes in the
483 atmospheric forcing also account for the variability of the upper ocean physical properties
484 and can have a cumulative effect over several years (Balmaseda et al., 2007; Böning et al.,
485 2006; Eden and Willebrand, 2001; Marsh et al., 2005).

486 The distribution of the water mass properties, the processes of vertical and horizontal mixing
487 and the circulation patterns in the Irminger and Iceland basins were described by García-Ibáñez
488 et al., 2016 and 2018. The poleward path of the ENACW (Pollard et al., 1996) and its mixing
489 with waters moving from the west across the NASPG (Ellett et al., 1986) accounted for the
490 highest subsurface temperature and salinity signals observed in the Iceland basin and even
491 more in the Rockall. The SPMW and LSW in the Rockall Trough exhibited higher temperature
492 and salinity signals in the respectively order of $\sim 1^{\circ}\text{C}$ and $\sim 0.05\text{-}0.1$ compared to the Irminger
493 and Iceland basins (Figure 4). The NASPG circulation patterns account for these differences
494 by transporting eastward these water masses, which subduct below the ENACW in the Rockall
495 Trough and mixed with warmer and more saline intermediate waters (i.e. Mediterranean
496 Water) moving from the south (e. g. Ellett et al., 1986; Harvey, 1982; Holliday et al., 2000).

497 The low temperature and salinity signals in the less-stratified Irminger basin (Figure 2)
498 experienced weaker interannual decreases in subsurface layers and higher rates of cooling and
499 freshening in intermediate and deep waters compared with the Iceland and Rockall basins
500 (Figure 4; Table 2). These longitudinal thermohaline heterogeneities were related to the
501 enhancement of vertical mixing processes in areas of water mass formation along the western
502 NASPG (Fröb et al., 2016; García-Ibáñez et al., 2015; Pickart et al., 2003; Piron et al., 2017)
503 and the water mass transformation along the NAC (Brambilla and Talley, 2008). The strongest
504 decrement in subsurface temperature and salinity along the Iceland and Rockall basins (Figure
505 4; Table 2) coincided with the significant event of heat loss and freshening observed by
506 Holliday et al., (2020) in the eastern NASPG over the period 2012-2016, so-called the Great
507 Salinity Anomaly. This pattern was not easily discernible in the Irminger basin due to the
508 transport of freshwater through the Fram Strait, as well as due the redirection of the Labrador
509 Current combined with changing wind stress curl (Holliday et al., 2020).



510 **4.2. Evaluation of the interannual trends in C_T in response to changes in C_{ant} and**
511 **C_{nat}**

512 The changes in the physical patterns observed in the NASPG influenced the interannual
513 variability of the MCS. The increase in C_T expected in the upper ocean due to the atmospheric
514 CO_2 uptake was offset by the cooling and freshening (and dealkalinization) of the subsurface
515 layers in the entire NASPG. The entrance of C_{ant} through the air-sea interface and its
516 accumulation dominated the observed increase in C_T , while the C_{nat} experienced a slightly
517 decrease throughout the region (Figure 5 and Table 2). A detailed description of the interannual
518 trends in C_T and A_T is provided in Appendix B.

519 The increase in the ventilation rates during this decade, shown by the negative AOU trends
520 (Figure S6 and Table S4), explained the higher growth in C_{ant} than expected due to the
521 atmospheric CO_2 increase. It leads an enhancement in the vertical mixing processes which
522 drove the transport of C_T -rich subsurface waters toward deeper areas and the slightly decrease
523 in C_{nat} through the whole water column. The trends of C_{ant} among the 2010s (0.85-1.77 μmol
524 $\text{kg}^{-1} \text{yr}^{-1}$; statistically significant at the 99% level) were higher than the observed on a decadal
525 to multidecadal scale since the late 20th century in the Irminger and Iceland basins (0.21-0.89
526 $\mu\text{mol kg}^{-1} \text{yr}^{-1}$ during 1991-2015, García-Ibáñez et al., 2016; and 0.38-1.15 $\mu\text{mol kg}^{-1} \text{yr}^{-1}$
527 during 1983-2013, Pérez et al., 2021), which suggest an enhancement in the C_{ant} accumulation
528 on interannual scales during periods of high ventilation, as previously reported by Perez et al.,
529 (2008).

530 The vertical distribution of C_{ant} and C_{nat} along the transect (Figure 3b and 3c) reflect the higher
531 stratification in the Iceland and Rockall basin compared with the well vertically-mixed
532 Irminger basin. It represents a source of variability in the interannual changes of C_{ant} among
533 the different layers and basins (Figure 4; Table 2). In the western NASPG, the surface heat loss
534 and enhanced deep convection processes favour the solubility and subsequent uptake of
535 atmospheric CO_2 and inject oxygenated and CO_2 -rich waters into deeper layers (Messias et al.,
536 2008). Its likely accounts for intermediate and deep layers in the Irminger basin exhibiting the
537 highest C_{ant} accumulation rates in the NASPG (Figure 5; Table 2). The highest ventilation of
538 the interior ocean in the Irminger basin was demonstrated by its minimum AOU values (Figure
539 2 and S6). It induced a rapid surface-to-bottom transport of C_{ant} shown by its highest rates of



540 increase in intermediate and deep waters throughout the region (Figure 5; Table 2). The high
541 C_{ant} values and its rapidly increment at DSOW were explained by the improved oxygenation
542 of this layer at shallower depths (interannual AOU trends given in Table S4) and its subduction
543 through the continental slope below ISOW.

544 In the eastern NASPG, the stratification weakened due to the path of the NAC warming
545 eastward the upper water column and accounted to slowdown the increase in C_{ant} in the Iceland
546 basin. An exception comes with the Rockall basin, in which the relatively warm and salty
547 ENACW (Figure 2 and 4) showed the maximum C_{ant} (58-68 $\mu\text{mol kg}^{-1}$) and minimum C_{T}
548 (2120-2131 $\mu\text{mol kg}^{-1}$) and C_{nat} (2058-2070 $\mu\text{mol kg}^{-1}$) throughout the region (Figure 3 and
549 5). The strong stratification of the Rockall Trough due to the wide differences in the physical
550 properties between the ENACW with SPMW and LSW plays a crucial role. The lower AOU
551 encountered in ENACW ($<20 \mu\text{mol kg}^{-1}$) compared with deeper layers ($>30 \mu\text{mol kg}^{-1}$) suggest
552 that the enhanced ventilation processes were limited to the subsurface layer increasing the
553 entrance of C_{ant} through the air-sea interface. The strong oxygenation, which reach the oxygen
554 saturation after 2014, could be related with the high rates of renovation of ENACW due to its
555 path from the south (Pollard et al., 1996) and its mixing with waters moving eastward (Ellett
556 et al., 1986). As the NAC transports nutrient-rich waters northward and eastward into
557 subsurface layers in the Rockall Trough, biological production tends to increase and actively
558 reduced the CO_2 excess from the ENACW (McGrath et al., 2012b), as proved by the observed
559 low C_{T} and C_{nat} . The strong interannual increase in the ENACW ventilation during this decade
560 increase the C_{ant} and decrease the C_{nat} (Rodgers et al., 2009) keeping approximately constant
561 the C_{T} (Table 3). The poorly ventilated thermocline (AOU $> 60 \mu\text{mol kg}^{-1}$), placed between
562 500-1000 m in the eastern NASPG, induced a C_{nat} -driven increase in C_{T} among the SPMW
563 and uLSW. However, its intrusion does not present relevant variations with time and thus does
564 not introduce differences in the interannual trends of the biogeochemical properties.

565 **4.3. Acidification trends**

566 The interannual pH_{T} trends (Figure 6, Table 2) exhibited the acidification of the whole water
567 column in NASPG during the period 2009-2019. Despite the acidification rates observed in
568 the most subsurface waters among the three basins were not significant at the 90% confidence
569 level (Table 2), they were consistent in the interval of 0.001 units yr^{-1} to those observed during



570 larger periods at time-series stations located across the North Atlantic: at subtropical latitudes
571 (0.0018 ± 0.0002 units yr^{-1} during 1995-2014 and 0.0020 ± 0.0001 units yr^{-1} during 1995-2023
572 at ESTOC, González-Dávila and Santana-Casiano, 2023; and 0.0017 ± 0.0001 units yr^{-1} during
573 1983-2014 at BATS, Bates et al., 2014) and subpolar latitudes (-0.0017 ± 0.0002 units yr^{-1} at
574 IRM-TS during 1983-2013 and -0.0026 ± 0.0002 units yr^{-1} at IS-TS during 1985-2013,
575 summarized by Pérez et al., 2021). In addition, the changes in the surface pH_T trends has been
576 reported by Leseurre et al., (2020) in the western NASPG within a wide latitudinal area (54-
577 64°N) during the period 2008-2017 in comparison with the periods 1993-1997 and 2001-2007.
578 Although the highly significant cooling observed in SPMW, the year-to-year variations in
579 ventilation (shown by the annual average AOU and its trends in Figure S6) and thus in C_{nat} and
580 C_{ant} (Figure 5), which could be related with fluctuations in the atmospheric forcing, introduced
581 relevant changes in pH_T on an interannual scale and explained the low significant trends. This
582 behaviour was clearly reflected in the Irminger basin, where strong slowdowns in ventilation
583 were observed from 2009 to 2010 and from 2013 to 2014, resulted in a relatively increase in
584 C_{nat} and decrease in C_{ant} observed in SPMW and extended with less intensity through the whole
585 water column.

586 The highest acidification rates were found through intermediate and deep waters in the
587 Irminger and Iceland basins, coinciding with the highest rates of increase in C_{ant} (Table 2,
588 trends statistically significant at more than 95% level of confidence). The exception comes
589 with the DSOW, which presented an interannual decrease in pH_T in phase with those of the
590 uLSW. This singularity was previously observed by García-Ibáñez et al., (2016), which noticed
591 the similar trends between the DSOW and LSW attributed to the recently formation and sink
592 through the continental slope of the DSOW. The acidification rates found among the uLSW,
593 LSW and ISOW (0.0026 - 0.0032 units yr^{-1}) experienced, on an interannual scale, an
594 acceleration in comparison with previous reported based on long-term records [e. g. 0.0009 -
595 0.0017 units yr^{-1} estimated for 1981-2008 by Vázquez-Rodríguez et al., (2012b); 0.0013 -
596 0.0016 units yr^{-1} estimated for 1991-2015 by García-Ibáñez et al., (2016); 0.0015 - 0.0019 units
597 yr^{-1} estimated for 1983-2013 at the IRM-TS by Pérez et al., (2021); 0.0019 ± 0.0001 units yr^{-1}
598 estimated for 1993-2017 by Leseurre et al., (2020)]. Contrasting the rates of change in pH_T
599 during the decade of study with those encountered by these multidecadal evaluations (and
600 considering the total amount of years comprising each of the studies and the changes in the ion



601 hydrogen concentration- $[H_T^+]$), we estimate an acceleration in the rates of acidification of 0.4-
602 5.4% in the Irminger basin and 1.0-9.0% in the Iceland basin during the 2010s since the late
603 20th century. This acceleration was mainly attributed to increased deep-water ventilation
604 (shown in the rapid decrease in AOU in Figure S6) favouring the progressively increase in the
605 accumulation of C_{ant} and C_{nat} toward intermediate a deep layers, in which cooling was not
606 significant in the Irminger basin and neither enough intense in both basins to compensate the
607 acidification.

608 Although the similarities encountered in the pH_T trends among both basins, the average values
609 presented differences which may be closely linked with the transport and transformations of
610 the water masses along the NASPG and mainly modulated by the Reykjanes Ridge (García-
611 Ibáñez et al., 2015, 2016, 2018). The transformation of the SPMW formed in the Iceland
612 (McCartney and Talley, 1982; Brambilla and Talley, 2008; Tsuchiya et al., 1992; Van Aken and
613 Becker, 1996) and flowing with the NAC across the Reykjanes Ridge (Brambilla and Talley,
614 2008) accounted for the lower pH_T values in the Irminger basin. The differences in pH_T found
615 at intermediate and deep layers were related with the divergence of the LSW path into two
616 cores when it reaches the Reykjanes Ridge (Álvarez et al., 2004; Pickart et al., 2003) and the
617 ISOW path flowing southward along the western Iceland basin and recirculated northward into
618 the eastern Irminger basin (Dickson and Brown, 1994; Saunders, 2001). These differences in
619 the spreading of water masses enhanced the ventilation in the Irminger basin favouring the fall
620 in pH_T compared with the Iceland basin. The rise in the ISOW following the Reykjanes Ridge
621 slope through its eastern flank favoured a strong vertical mixing over and around the ridge
622 (Ferron et al., 2014) and a reduction of the LSW core in the Iceland basin (García-Ibáñez et
623 al., 2015), contributing to resemble pH_T values and trends among the uLSW and LSW in this
624 basin.

625 The upper waters of the Rockall Trough presented the maximum pH_T throughout the transect
626 (8.02-8.08 units). The observed strong pH_T fluctuations between years related with interannual
627 changes in the NAC do not allow to discern trends with a statistically interval of confidence
628 equal or higher than the 90% on a decadal scale. The interannual decrease in pH_T in the
629 ENACW (~ 0.001 units yr^{-1}) was half than the observed along southernmost transects in the
630 Rockall Trough between 1991 and 2010 (~ 0.002 units yr^{-1} , McGrath et al., 2012a). The



631 temporal distribution of the average pH_T (Figure 6) highly influenced by changes in the
632 ventilation (seen in AOU trends in Figure S6) allow to discern two periods: the approximately
633 constant ventilation rates keep a steady state in terms of pH_T during 2009-2011, while the
634 progressively renewal of oxygenated water after 2012 (and peaking in this year) increase the
635 pH_T . The year-to-year variability in the biogeochemical patterns after 2012 may be attributed
636 to the fluctuations in the spreading into the Rockall Trough of several water masses occupying
637 different depths coming from the south and east (Ellett et al., 1986; Pollard et al., 1996). This
638 contributed to enhance the oxygenation of the ENACW during the 2010s (seen in minimum
639 AOU values highly variables between years and which tend to decrease with 99% statistical
640 confidence; Figure S6 and Table S4) and the reduction of the injection of saline subsurface
641 waters from subtropical latitudes (Holiday et al. 2020). The findings suggest that the strong
642 decrease in A_T (Figure S4 and Table S4) due to the freshening and weak increase in C_T (Figure
643 5 and Table 2) due to enhanced ventilation counteract the acidification in the ENACW. The
644 SPMW among the Iceland and Rockall basins showed similar pH_T trends (Table 2) due to the
645 emplacement of the poorly-oxygenated thermocline at these depths (García-Ibáñez et al.,
646 2016). The approximately constant AOU at SPMW in the eastern NASPG (Figure S6) proved
647 its steady ventilation, which can introduce differences in the acidification rates among the
648 layers accomplishing the Rockall Trough. The influence of the cooling and freshening of
649 deeper areas due to the spreading and horizontal mixing was notable in the LSW, which
650 presented slightly higher pH_T values in the Rockall respect to the adjacent Iceland basin.

651 4.4. Drivers pH

652 Due to the variety of processes involved in OA, a decomposition of the pH_T trends into the
653 individual components that govern its spatio-temporal variability was done (see section 2.2.5).
654 The interannual pH_T changes ($\frac{dpH_T}{dt}$) explained by fluctuations in temperature ($\frac{\partial pH_T}{\partial T} \frac{\partial T}{dt}$), salinity
655 ($\frac{\partial pH_T}{\partial S} \frac{\partial S}{dt}$), A_T ($\frac{\partial pH_T}{\partial A_T} \frac{\partial A_T}{dt}$) and C_T ($\frac{\partial pH_T}{\partial C_T} \frac{\partial C_T}{dt}$) were calculated for each layer and basin (Eq. 2) and
656 summarized in Table 3. The positive contributions of each of the drivers indicate an increase
657 in pH_T while negative contributions the opposite. The cumulative pH_T change resulting from
658 the distinct drivers ($\frac{dpH_T}{dt}$ (calculated) in Table 3) were consistent with the observed pH_T trends
659 ($\frac{dpH_T}{dt}$ (obs) in Table 3, discussed in section 4.2), thereby instilling confidence in the
660 methodology. The minimal differences between observed and calculated rates of change have



661 added coherence to the non-significant trends identified for pH and its drivers in some basins
662 and layers (Table 2, 3 and S4). In the entire section at SPMW, the $\frac{dpH_T}{dt}$ (calculated), explained
663 by the cumulative impact of its drivers (all of them statistically significant at the 95% level of
664 confidence), aligns within a range of <0.0002 units yr^{-1} with $\frac{dpH_T}{dt}$ (obs) (which was not
665 significant). In the Irminger and Iceland basins at intermediate and deep layers, the $\frac{dpH_T}{dt}$ (obs)
666 (statistically significant at least at the 95% level of confidence) were consistent within the
667 range of <0.001 units yr^{-1} with $\frac{dpH_T}{dt}$ (calculated) (T, S and NA_T shows non-significant trends at
668 some of the intermediate and deep layers). The interannual variations were non-significant for
669 pH_T neither for its drivers in the Rockall Trough at LSW and ENACW. The high temporal
670 dispersion of average data in these layers was mainly related to the rise in depth of LSW along
671 the eastern continental slope and its mixing with shallower waters coming from subtropical
672 latitudes (Ellett et al., 1986; Harvey, 1982; Holliday et al., 2000). The substantial variability
673 introduced by these processes made it difficult to discern the pattern of acidification and its
674 drivers on an interannual scale in the shallow Rockall Trough. Therefore, long-term monitoring
675 and the development of multidecadal-scale studies are required in this area to derive significant
676 conclusions.

677 The cooling and freshening of the NASPG during the 2010s modified the physical-driven pH_T
678 changes compared with those encountered by García-Ibáñez et al., (2016) during previous
679 decades in the western NASPG. The cooling contributed to increase the pH_T and compensated
680 the observed acidification rate. The increase in pH_T due to temperature fluctuations was
681 maximum at SPMW (~ 0.001 units yr^{-1}) and was reduced an order of magnitude to negligible
682 toward intermediate and deep layers (<0.0003 units yr^{-1} at uLSW and below). The increase in
683 pH_T due to salinity fluctuations was minimal (<0.0001 units yr^{-1}) through the whole water
684 column in the three basins, reflecting that the observed freshening caused insignificant changes
685 in pH_T . The temperature and salinity contributed by 19.1-26.5% and 1.2-3.3%, respectively, in
686 the total pH_T change in the upper layers, while presented an influence three times lower in
687 intermediate and deep layers (1.3-7.6% and $<0.6\%$, respectively). The enhanced convective
688 processes in the Irminger basin (e. g. Fröb et al., 2016; García-Ibáñez et al., 2015; Gladyshev
689 et al., 2016a, 2016b; Piron et al., 2017) together with the rapid transport of LSW from the
690 Labrador Sea to the Irminger basin (Yashayaev et al., 2007) introduced differences in the



691 thermal-driven pH_T with the Iceland basin which has been previously reported by García-
692 Ibáñez et al., (2016). The advection of LSW through the Greenland continental slope also
693 affected the DSOW (Read, 2000; Yashayaev and Dickson, 2008), which shows thermal-driven
694 pH_T changes consistent with those encountered through the LSW in the Irminger basin.

695 Despite the negligible direct contribution of the salinity fluctuations over the pH_T changes, the
696 freshwaters fluxes influence the distribution of A_T and C_T indirectly affecting pH_T trends. Once
697 removed the effect of salinity by normalization (Pérez et al., 2021), the positive NA_T trends
698 encountered in the upper layers lead a rise in pH_T , while the diminished NA_T contributed to
699 decrease the pH_T toward the interior ocean. The changes in NA_T described the 7.8-10.1% of
700 the total pH_T change at SPMW. The NA_T -driven pH_T changes became insignificant with depth
701 (Table 3) due to the insignificantly interannual changes in NA_T through LSW and ISOW (Table
702 S4). The weak contribution of NA_T in these layers (1.3-5.1%) could be related to the difficulty
703 of reversing the large alkalization until the 2000s resulted from the slowdown in the
704 formation of LSW since the mid-90s (Lazier et al., 2002; Yashayaev, 2007), which was
705 transmitted towards deeper overflow waters (Sarafanov et al., 2010). The substantial
706 interannual changes and the abrupt change between periods of increase and decrease of the
707 seawater properties at DSOW (Yashayaev et al., 2003; Stramma et al., 2004) linked with
708 changes in the LSW formation (Dickson et al., 2002) explained the rapidly decrease in NA_T
709 (Table S4), which described the 14.6% of the pH_T declining.

710 The increase in NC_T drove by the rise in C_{ant} was found to govern the acidification, with a
711 contribution higher than the 67% in the whole water column throughout the region. The NC_T -
712 driven pH_T declining was close to twice the observed and calculated acidification rates through
713 the SPMW (Table 3). However, the contribution of NC_T at SPMW (67-69%) was lower than
714 the encountered toward the interior ocean (82-96%) due to the relevance of temperature and
715 A_T over pH_T trends in the upper ocean. The cooling and increase in NA_T counteracted the
716 acidification expected by the increasing C_T at SPMW by 28-34% and 11-15%, respectively.
717 The weaker cooling through the intermediate and deep layers leads a lower thermal-
718 neutralization of the C_T -driven acidification (1.5-9.3%), while the decreasing NA_T contributed
719 to decrease the pH_T by < 2-12% in the uLSW, LSW and ISOW and by ~15% in the DSOW.
720 The driver analysis also remarked that the role of freshening in counteract the acidification



721 was small in the upper layers (<6%) and becoming insignificant toward the interior ocean
722 (<2%).

723 **4.5. Interannual changes in Ω_{Ca} and Ω_{Arag}**

724 The analysis of the changes in Ω_{Ca} and Ω_{Arag} hold significance in elucidating the potential
725 effects of OA over the $CaCO_3$ species calcite and aragonite, thereby offering insights into their
726 potential implications for marine calcifying organisms and ecosystems. The vertical
727 distribution of Ω_{Ca} and Ω_{Arag} is presented in Figure S3. The upper and intermediate layers up
728 to 2100-2400 m depth of the Irminger and Iceland and the whole Rockall basin were
729 supersaturated for aragonite ($\Omega_{Arag} > 1$), while the DSOW was undersaturated ($\Omega_{Arag} < 1$). The
730 ISOW, with Ω_{Arag} ranged between 1.0 and 1.1 at the beginning of the decade, crossed to
731 undersaturated conditions at the end of the period due to the progressively rise of the aragonite
732 saturation horizon (depth in which $\Omega_{Arag} = 1$). The whole water column throughout the section
733 was supersaturated for calcite ($\Omega_{Ca} > 1$) due to its lower solubility (Mucci, 1983). The Ω_{Ca} and
734 Ω_{Arag} in the SPMW (2.2-2.7 and 1.4-1.7 units, respectively) were lower than the encountered
735 equatorward in the subsurface Atlantic (>4.0 and >2.5 units, respectively; González-Dávila et
736 al., 2010; González-Dávila and Santana-Casiano, 2023). The poleward pathway of low-
737 latitude upper waters through the Rockall Trough explained the higher Ω_{Ca} and Ω_{Arag} found in
738 the ENACW (3.0-3.6 and 1.8-2.3 units, respectively). The reduction in Ω_{Ca} and Ω_{Arag} towards
739 higher latitudes in upper and intermediate layers smooth the vertical gradients in the NASPG
740 compared with the subtropical latitudes (González-Dávila et al., 2010; González-Dávila and
741 Santana-Casiano, 2023).

742 The interannual trends in Ω_{Ca} and Ω_{Arag} (Figure 7, Table 2) exhibited the decrement through
743 the whole water column along the NASPG with a level of statistical confidence generally
744 higher than the 90%. The rates of declining for Ω_{Ca} and Ω_{Arag} in the SPMW (0.011-0.021 and
745 0.007-0.013 units yr⁻¹; respectively) were consistent with the trends observed up to 100 m
746 depth at ESTOC between 1995 and 2023 (0.019 ± 0.001 and 0.012 ± 0.001 units yr⁻¹,
747 respectively; González-Dávila and Santana-Casiano, 2023) and in surface waters at the IS-TS
748 between 1985 and 2008 (0.0117 ± 0.0011 and 0.0072 ± 0.0007 units yr⁻¹, respectively;
749 Olafsson et al., 2009). The declining in Ω_{Arag} in the SPMW accelerated by ~26% and ~51% in
750 the Irminger and Iceland basins, respectively, in comparison with the trends given for the



751 period 1991-2018 (0.0052 ± 0.0006 and 0.0049 ± 0.0015 units yr^{-1} , respectively; García-Ibáñez
752 et al., 2021). The observed decrease in Ω_{Arag} in the SPMW was $\sim 23\%$ faster in the Rockall
753 Trough than in the adjacent Iceland basin. The interannual declining for Ω_{Ca} and Ω_{Arag} in the
754 ENACW (0.012 and 0.008 units yr^{-1} , respectively) agreed with these previous observations but
755 were not statistically significances likely due to the high variability modifying the changes in
756 pH_T in this layer (see section 4.2). Despite the acceleration of the acidification rates toward
757 intermediate and deep layers, the declining rates weakened for Ω_{Ca} and even more for Ω_{Arag}
758 (Table 2). Moreover, the vertical profiles were approximately constant throughout the section
759 in contrast with the heterogeneous vertical distribution of pH_T between basins. This behaviour
760 was previously observed in the Irminger and Iceland basins by García-Ibáñez et al., (2021) and
761 explained by pressure and temperature-induced changes in the speciation of the CO_2 -carbonate
762 chemistry species (Jiang et al., 2015) and in the solubility of calcite and aragonite (Mucci,
763 1983). Their combined action counterbalanced the alterations in Ω resulting from acidification,
764 particularly in colder deep waters where the solubility of calcite and aragonite was reduced
765 (García-Ibáñez et al., 2021). However, the fall down in Ω_{Ca} and Ω_{Arag} along the uLSW, LSW
766 and ISOW accelerated by 40-75% in relation with the trends reported by García-Ibáñez et al.,
767 (2021) for the Irminger and Iceland basins. The LSW and ISOW presented faster declining
768 rates for Ω_{Ca} and Ω_{Arag} in the Irminger (Table 2), which may be caused by the enhanced
769 ventilation of the interior ocean which accelerated the acidification (see section 4.2). The
770 westward rise in depth of these layers along the Greenland continental slope, accompanied by
771 a subsequent elevation in the horizons of solubility, resulted in reduced buffering capacity
772 against acidification effects in the Irminger basin when compared to the Iceland basin. In
773 contrast, the rise in depth of LSW in the Rockall Trough favour the increment of ~ 0.2 units in
774 Ω_{Ca} and Ω_{Arag} with respect to the Iceland basin but had not influence on the interannual
775 trends, which were coinciding. The Ω_{Ca} and Ω_{Arag} in the DSOW, despite showed a trend
776 accelerated by $\sim 30\%$ compared to the observed by García-Ibáñez et al., (2021), presented the
777 weakest interannual decreases throughout the section (0.004 ± 0.003 and 0.002 ± 0.001 units
778 yr^{-1} , respectively) due to the high pressure and low temperatures compensating the rapidly
779 acidification (Figure 6, Table 2).

780 A driver analysis enabled the assessment of the impact of individual processes involved in OA
781 on the variations in Ω_{Ca} and Ω_{Arag} (see section 2.2.6). The correlation of Ω with pH_T ($r^2=0.90$)



782 with a level of significance higher than the 99% explained that the individual components
783 driving OA accompanied the declining in Ω . The interannual Ω variations ($\frac{d\Omega}{dt}$) explained by
784 fluctuations in temperature ($\frac{\partial\Omega}{\partial T} \frac{\partial T}{dt}$), salinity ($\frac{\partial\Omega}{\partial S} \frac{\partial S}{dt}$), A_T ($\frac{\partial\Omega}{\partial A_T} \frac{\partial NA_T}{dt}$) and C_T ($\frac{\partial\Omega}{\partial C_T} \frac{\partial NC_T}{dt}$) were calculated
785 for each layer and basin (Eq. 5) and summarized in Table 4. The sum of changes in Ω due to
786 the distinct drivers ($\frac{d\Omega}{dt}$ (calculated) in Table 4) agreed with observed Ω trends ($\frac{d\Omega}{dt}$ (obs) in Table
787 4) in all the basin and layers except for the DSOW, in which the strong NA_T decrease had a
788 crucial influence on declining Ω . The driver analysis, as mentioned when was applied for pH_T ,
789 contributes to add coherence and consistency to those non-significant trends identified and/or
790 its drivers in some basins and layers (Table 2, 3 and S4)

791 The C_{ant} -driven rise in NC_T governed the decrease in Ω with a contribution of 79-83% in the
792 SPMW which reached $\sim 97\%$ toward deeper waters. The increase in NA_T in the SPMW
793 accounted by 10.4-13.0% in the Ω trends and counteracted its NC_T -driven decrease by 12.6-
794 16.2%. The contribution of NA_T fall and reversed toward deeper waters, explained $<6\%$ of the
795 decline in Ω in the uLSW, LSW and ISOW in the Irminger basin and $<11\%$ in the Iceland
796 basin. The pronounced impact of the rapid decrease in NA_T on the acidification of the DSOW
797 (see section 4.3) depicted the greater contribution of NA_T encountered among the Irminger
798 basin (16%) and compensated the C_T -driven decrease in Ω by 36.4%. In the Rockall Trough,
799 the contribution of NC_T changes on Ω was reduced at LSW (78.2-79.0%) compared to the
800 Irminger basin (94.5%) while the effect of NA_T fluctuations tripled until reach 12.6-12.7%.

801 Despite the evaluated crucial role of cooling in counteracting the acidification, the temperature
802 fluctuations have an opposite effect on Ω owing to the thermodynamic relationship inherent in
803 the acid-base equilibrium of the CO_2 -carbonate system (Dickson and Millero, 1987). In the
804 Irminger and Iceland basins, the observed decreasing temperatures negligibly contributed to
805 fall down the Ω (3.6% in the SPMW and $<2\%$ in intermediate and deep waters). The influence
806 of salinity, as occurred with the pH_T trends, was minimal: the observed freshening contributed
807 to elevate the Ω trends and compensated its declining by 4.6-4.7% at SPMW, 1.1-2.1% at
808 uLSW and LSW and 0.5-1.2% at ISOW and DSOW. Even the slightly faster cooling and
809 freshening observed in the Rockall Trough, the contributions of temperature and salinity on
810 the Ω did not exceed the 7% in each of its layers.



811 The driver analysis exhibited the strongest interannual decrease in Ω in the upper layers
812 governed by the uptake of C_{ant} weakly compensated by the increase in NA_T and favoured by
813 the cooling and freshening. The decrease in Ω could have severe consequences on organisms
814 reliant on aragonite, which is less resistant to dissolution than calcite (Mucci, 1983; Broecker
815 and Peng, 1983) and thus expected to experience relatively higher susceptibility to the effects
816 of OA over shorter time scales (Raven et al., 2005). The progressive reduction in Ω_{Arag} is
817 driving a long-term decrease in the depth of the aragonite saturation horizon ($\Omega_{\text{Arag}}=1$) by 80-
818 400 m since the preindustrial era (Álvarez et al., 2003; Feely et al., 2004; Pérez et al., 2013,
819 2018; Pérez et al., 2013; Tanhua et al., 2007; Wallace, 2001) and is projected to shoal by more
820 than 2000 m by the end of the century under the IS92a scenario (Orr et al., 2005). Likewise,
821 Orr et al., (2005) suggested that high-latitudes surface waters could become undersaturated
822 when the atmospheric CO_2 concentration double the preindustrial concentration within the
823 next 50 years. It would reduce the calcification rates in some shallow calcifying organism by
824 more than the 50% (Feely et al., 2004).

825 The planktonic aragonite-producers pteropods (e. g. *Limacina helicina*, *Clio pyramidata*),
826 which have high population densities in subpolar regions up 300 m depth (Bathmann et al.,
827 1991; Urban-Rich et al., 2001) and play a key role in the export flux of both carbonate and
828 organic carbon (Accornero et al., 2003; Collier et al., 2000), are expected to be highly
829 vulnerable to OA if the aragonite saturation horizon continue to shoal (Orr et al., 2005). The
830 undersaturation toward intermediate and upper layers negatively influence the aragonite-based
831 CWC (e. g. *Lophelia pertusa*, *Madrepora oculata*), which show their highest diversity and
832 population along the NASPG between 200 and 1000 m depth among the global ocean (Roberts
833 et al., 2009). In fact, several studies reported that CWC ecosystems are anticipated to be among
834 the first deep-sea ecosystems to experience acidification threats (Guinotte et al., 2006; Maier
835 et al., 2009; Raven et al., 2005; Roberts et al., 2009; Turley et al., 2007), particularly in the
836 North Atlantic (Perez et al., 2018). The findings presented here contribute to a deeper
837 understanding of the biological impacts of OA along the NASPG.

838 5. Conclusions

839 This research has evaluated the interannual changes in the basin-wide CO_2 -carbonate system
840 dynamics along the NASPG during the 2010s. Despite the observational period is relatively



841 short to quantify long-term trends and to formulate significant future projections, the finding
842 has allowed to evaluate the ocean response, in terms of carbonate system dynamics and on an
843 interannual scale, to changes in deep-water convection and to isolate events affecting the
844 physical patterns. The present study improved the comprehension of how the processes
845 modifying the rates of accumulation of C_{ant} and acidification on an interannual scale could
846 have a relevance impact on its decadal and multidecadal trends.

847 The assessment of OA within the Irminger and Iceland basins was enhanced by supplying
848 novel data and trends spanning a decade in which the physical patterns reversed. Additionally,
849 the study provides an unprecedented analysis of the physico-chemical variations in the Rockall
850 Trough, which is crucial for the assessment of the entire longitudinal span of the NASPG and
851 advancing our understanding of OA in the North Atlantic and Global Ocean. The data and
852 results given in this article could be used for modelling and compared with other repeated
853 hydrographic section data at mid and high latitudes in the North Atlantic, such as the A02,
854 A25, AR07E and AR28 framed in the GO-SHIP program, as well as used in conjunction to
855 develop future studies focused on the transport of C_{ant} -loaded and acidified waters. The
856 observational period is relatively short to quantify long-term trends and to formulate
857 significant future projections. The acceleration in surface warming and consequent changes in
858 $f\text{CO}_2$ and pH observed during 2010s may be linked to isolated extreme events such as marine
859 heat waves and are not necessarily indicative of prolonged behaviours over time.

860 Overall, the entrance and accumulation of C_{ant} and interannual acidification trends were
861 strongly affected by the cooling, freshening and enhancement in the oxygenation of the whole
862 water column during the 2010s. The interannual acidification trends ranged between 0.0013
863 and 0.0032 units yr^{-1} in the Irminger basin, 0.0023 and 0.0029 units yr^{-1} in the Iceland basin
864 and 0.0006 and 0.0024 units yr^{-1} in the Rockall Trough. The convective processes increased
865 the accumulation rates of C_{ant} in the interior ocean by 50-86% and accelerated the acidification
866 rates by around 10% compared to previous decades in the Irminger and Iceland basins. In the
867 eastern NASPG, the shallower hydrography of the Rockall Trough and the poleward
868 circulation patterns accounted for differences in the acidification rates respect to surrounding
869 waters. The high variability of this area explained the non-significant trends at interannual
870 timescales and support the necessity of assess the evolution of its carbonate system properties



871 over larger time periods. However, the low NA_T content of ENACW due to the spreading of
872 subtropical subsurface waters into higher latitudes was suggested as the main process
873 decelerating the acidification trends in the upper Rockall Trough. The improved oxygenation
874 of LSW decreasing the C_{nat} and thus compensating the C_{ant} -driven increase in C_T may
875 contributed to slowdown the declining in pH_T in relation to the Iceland basin. The acidification
876 of the NASPG was accompanied by a decline in the Ω_{Ca} and Ω_{Arag} of 0.004-0.011 and 0.003-
877 0.009 units yr^{-1} , respectively, in the Irminger basin; 0.007-0.016 and 0.005-0.010 units yr^{-1} ,
878 respectively, in the Iceland basin; and 0.008-0.021 and 0.005-0.013 units yr^{-1} , respectively, in
879 the Rockall Trough.

880 The rise in NC_T , mainly explained by the increasing uptake of C_{ant} , was found to govern the
881 acidification of the NASPG with a contribution ranged between 53% and 68% in the upper
882 water column and higher than 82% toward the interior ocean. The increase in NC_T was also
883 the main driver of Ω_{Ca} and Ω_{Arag} trends, with contributions higher than 82% in the Irminger
884 basin, 79% in the Iceland basin and 64% in the Rockall Trough. The combined effect of the
885 decreasing temperature, salinity and NA_T neutralized the 45-49% of the C_T -driven acidification
886 along the entire longitudinal span of the SPMW. The cooling drove this compensation (27-
887 50%) followed by the decrease in NA_T (11-33%), while the freshening had a minimal influence
888 (<6%). The deep-water ventilation processes slowdown the cooling and freshening toward the
889 interior ocean in the Irminger and Iceland and drove the progressively interannual increase in
890 NA_T . Thus, the NA_T contributed to acidification by <11% within the intermediate and deep
891 layers and the physical counteraction of the C_T -driven acidification fall to <10%. In contrast,
892 the cooling weakly promoted the decline in Ω (<7% in the upper water column and <2% toward
893 the interior ocean), being only efficiently counteracted in subsurface layers by the increase in
894 NA_T (12-16%) and the freshening (3-5%).

895 The present investigation pretended to emphasize the progressively increase in the uptake and
896 accumulation of C_{ant} and subsequent acceleration of OA along the NASPG. The longitudinal
897 span of the NASPG and the differences in circulation patterns, water masses and bathymetry
898 along the section behave as a relevant source of spatio-temporal variability. The enhanced
899 convective processes in the western NASPG were found to favour the entrance of C_{ant} in
900 intermediate and deep-layers and this its acidification, as well as influence the carbonate



901 system dynamics in the eastern NASPG. The advancement of comprehensive basin-wide
902 longitudinal evaluations, as the presented here, facilitates a more accurate understanding of the
903 mechanisms dictating basin-scale acidification processes. Furthermore, this promotes the
904 improvement of the projections pertaining to the future state of the oceans run by models and
905 forecast. Considering the important variability in the mechanism controlling the distribution
906 of the physico-biogeochemical properties and particularly the OA in the North Atlantic, this
907 research aims to highlight the necessity of continue monitoring and sampling the whole water
908 column through repeated hydrographic sections, especially through the highly variable but less
909 assess easternmost part.

910 **Appendix A: Correction of Dissolved Oxygen records for the cruise of 2019**

911 The sensor-measured DO data for the cruise of 2019 were corrected by considering the DO
912 output data given by the neural network ESPER_NN (Carter et al., 2021) for the cruises of
913 2016 and 2019 (hereinafter ESPER-estimated DO) and the WINKLER-measured DO during
914 the cruise of 2016. Among the 16 equations provided by the ESPER_NN that differently
915 combines seawater properties as predictors, we use the equation 8 which only need as inputs
916 the T and S (due to lack of measured macronutrients during the cruise of 2019) along with
917 latitude, longitude, depth and date (see Table 2 in Carter et al., 2021). The reported Root Mean
918 Squared Error (RMSE) of equation 8 for DO estimations in the global ocean is $\pm 9.7 \mu\text{mol kg}^{-1}$,
919 which is reduced for intermediate waters (1000-1500 m) to $\pm 5.9 \mu\text{mol kg}^{-1}$ (see Table 7 in
920 Carter et al., 2021). Additionally, a new set of DO for 2019 based on WINKLER data for 2016
921 was computed, which was referred in this study as “pseudo-WINKLER” data. The difference
922 between WINKLER-measured and ESPER-estimated DO during 2016 was interpolated to the
923 longitudes and depths of the samples of 2019 by applying Delaunay Triangulation. The
924 pseudo-WINKLER data was described as the sum of these interpolated differences and the
925 ESPER-estimated DO data for 2019. The longitudinal distribution of measured and ESPER-
926 estimated DO data for 2016 and 2019 is depicted in Figure S1a and S1b. The interpolated
927 pseudo-WINKLER data for the cruise of 2019 were included in Figure S1a.

928 The sensor records of DO in 2019 were in average $4.90 \mu\text{mol kg}^{-1}$ lower than the ESPER-
929 estimated and $10.31 \mu\text{mol kg}^{-1}$ lower than the pseudo-WINKLER. A higher discrepancy was
930 observed in the average sensor-measured DO in the east part ($237.60 \pm 15.00 \mu\text{mol kg}^{-1}$)



931 compared with the west part ($281.40 \pm 14.75 \mu\text{mol kg}^{-1}$). The average differences (measured
932 minus ESPER-estimated DO and measured minus pseudo-WINKLER DO, $\Delta\text{DO}_{\text{meas-ESPER}}$ and
933 $\Delta\text{DO}_{\text{meas-pseudoWINKLER}}$, respectively; Figure S2c and S1d) shows that the sensor records were
934 strongly underestimated in the east part (-20.98 ± 10.91 and $-28.77 \pm 12.60 \mu\text{mol kg}^{-1}$,
935 respectively) and weakly overestimated in the west part (8.59 ± 8.53 and $5.18 \pm 12.02 \mu\text{mol}$
936 kg^{-1} , respectively) during the cruise of 2019. These differences were corrected separately west
937 and east of 21.5°W by using the relationship $\frac{\Delta\text{DO}_{\text{meas-pseudoWINKLER}}}{\text{measured DO}}$. The averages of this
938 relationship in the west and east part of the transect (0.016 and $-0.12 \mu\text{mol kg}^{-1}$, respectively)
939 were used as corrector factors. The corrected DO values were given by the product between
940 the measured DO and $\left(1 - \frac{\Delta\text{DO}_{\text{meas-pseudoWINKLER}}}{\text{measured DO}}\right)$.

941 **Appendix B: Interannual trends of C_T , NC_T , A_T and NA_T**

942 The observed rates of increase in C_T (Table 2) did not show notable differences with respect
943 to the interannual trends determined from previous decades at the Irminger and Iceland basins
944 (0.62 - 0.82 and 0.38 - $0.64 \mu\text{mol kg}^{-1} \text{yr}^{-1}$, respectively; García-Ibáñez et al., 2016) and at IRM-
945 TS and IS-TS (0.49 - 0.71 and 0.39 - $0.94 \mu\text{mol kg}^{-1} \text{yr}^{-1}$, respectively; Pérez et al., 2021). The
946 interannual rates of increase in NC_T were higher than those of C_T in the subsurface layers,
947 while the trends were similar among intermediate and deep layers (Table 2).

948 The interannual trends of A_T (Figure S4 and Table S4) was found to be highly impacted by
949 freshening, with decreasing rates ranging from -0.33 to $-0.71 \mu\text{mol kg}^{-1} \text{yr}^{-1}$ among the
950 SPMW and ENACW and from -0.01 to $-0.18 \mu\text{mol kg}^{-1} \text{yr}^{-1}$ within the uLSW, LSW, ISOW
951 and DSOW. It contrasts with the minimal interannual changes and slight rates of increase in
952 A_T encountered among the different layers by García-Ibáñez et al., (2016) from 1991 to 2015
953 in the Irminger basin (between 0.10 and $0.28 \mu\text{mol kg}^{-1} \text{yr}^{-1}$) and Iceland basin (between -
954 0.04 and $0.07 \mu\text{mol kg}^{-1} \text{yr}^{-1}$), and with the trends reported for the period 1983-2013 by Pérez
955 et al., (2021) at the IRM-TS (between 0.13 and $0.22 \mu\text{mol kg}^{-1} \text{yr}^{-1}$) and at the IS-TS (between
956 -0.04 and $0.15 \mu\text{mol kg}^{-1} \text{yr}^{-1}$). These heterogeneities in the temporal evolution of the A_T were
957 driven by the decadal salinification of the whole water column observed since the late 20th
958 century and interrupted by interannual freshening episodes such as during the 2010s.



959 The interannual NA_T trends reversed in comparison with those of A_T along the SPMW and
960 ENACW (Figure S4 and Table S4). This increment in NA_T was related with the stagnation of
961 A_T -rich subtropical waters in the upper layers due to the slowdown of the NASPG since the
962 mid-90s (e. g. Böning et al., 2006; Häkkinen and Rhines, 2004).

963 Code Availability

964 MATLAB and R codes for CANYON-B are available at
965 <https://github.com/HCBScienceProducts/CANYON-B>. MATLAB and R code for ESPER_NN
966 are available at <https://github.com/BRCScienceProducts/ESPER>. MATLAB code for
967 anthropogenic carbon calculation is available at
968 http://oceano.iim.csic.es/_media/cantphict0_toolbox_20190213.zip. The CO₂SYS programme
969 for MATLAB is available at <https://github.com/jonathansharp/CO2-System-Extd>.

970 Data Availability Statement

971 The measured surface-to-bottom CLIVAR data (2009-2019) used in this investigation are
972 published in open-access at Zenodo (DOI: 10.5281/zenodo.10276221). The GO-SHIP A25-
973 OVIDE data for the cruise of 2018 is available at SEANOE
974 (<https://www.seanoe.org/data/00762/87394/>).

975 Author contribution

976 DCH contributed with data analysis and wrote the manuscript. FFP, DCH, AV, DGS, AGG,
977 MGD and JMSC worked on the design, conceptualization and data preparation. SG, AS, MGD,
978 JMSC, AGG and DGS participated in 8, 4, 7, 7, 2 and 2 cruises, respectively. SG and AS were
979 the Chief Scientist in all cruises and responsible for the operational and maintenance
980 procedures for the CTD and additional sensors and thus for physical and sensor-measured
981 variables. MGD and JMSC got the funding acquisition and provision of resources for the
982 Spanish team from the ULPGC. SG and AS got the funding for ship time and provision of
983 resources for all the cruise participants. All authors critically revised the manuscript.

984 Competing interest

985 The authors declare that the research was conducted in the absence of any commercial or
986 financial relationships that could be construed as a potential conflict of interest.

987 Acknowledgement

988 The participation on the cruises for the Spanish Team from the ULPGC was funded by the
989 Science Spanish Ministry under the Complimentary Actions CTM2008-05255, CTM2010-
990 09514-E and CTM2011-12984-E (years 2009-2011), the FP7 European project



991 CARBOCHANGE under grant agreement no. 264879 and by the Spanish Innovation and
992 Science Ministry through the Projects EACFe (CTM2014-52342-P) and ATOPFe (CTM2017-
993 83476-P). SG and AS were supported by FMWE-2023-0002. FFP and AV were supported by
994 the BOCATS2 (PID2019-104279GB-C21) project funded by
995 MCIN/AEI/10.13039/501100011033 and by EuroGO-SHIP project (Horizon Europe
996 #101094690). The participation of DCH was funded by the PhD grant PIFULPGC-2020-2
997 ARTHUM-2. Special thanks go to the technician and researchers Adrian Castro Álamo (2
998 cruises), Anna Barrera Galderique (3 cruises), Rayco Alvarado Medina (2 cruises) and Pilar
999 Aparicio Rizzo (1 cruise) who helped with in situ analysis. We also thanks technicians at the
1000 P. P. Shirshov Institute of Oceanology from the Russian Academy of Science for the in situ
1001 analysis of dissolved oxygen and nutrients.



1002 Legend for figures

1003 Figure 1. (a) Map of the North Atlantic Subpolar Gyre (NASPG) with the schematic diagram
1004 of the surface and deep circulation patterns compiled from Lherminier et al., (2010); Pérez et
1005 al., (2021); Sarafanov et al., (2012); Schmitz and McCartney, (1993); Schott and Brandt,
1006 (2007) and Sutherland and Pickart, (2008). The acronyms are defined as follow: the
1007 bathymetric features are shown in grey (RR: Reykjanes Ridge, HB: Haton Bank, GBB: George
1008 Bligh Bank, CGFZ: Charlie-Gibbs Fracture Zone, GIR: Greenland-Iceland Ridge, and GSR:
1009 Greenland-Scotland Ridge), the surface currents are shown in orange (NAC: North Atlantic
1010 Current, and IC: Irminger Current) and the deep water circulation is shown in blue and purple
1011 (ISOW: Iceland-Scotland Overflow Water, DSOW: Denmark Strait Overflow Water, LSW:
1012 Labrador Sea Water, and DWBC: Deep Western Boundary Current). The longitudinal
1013 distribution of the surface-to-bottom sampling stations along the cruise track of 2016 (repeated
1014 throughout the cruises) is shown with red dots. The black lines along the cruise track delimited
1015 the three basins. (b) Vertical distribution of the water masses considered in this study for each
1016 of the basins. The isopycnals, plotted over the salinity distribution for the cruise of 2016, show
1017 the limits of the layers and were defined by potential density (in kg m^{-3}) referred to 0 dbar (σ_0).
1018 The vertical gray lines show the limits between basins. The acronyms of the water masses and
1019 the selection of potential density values delimiting the layers are detailed in section 2.2.4.
1020 Figure produced with Ocean Data View (Schlitzer, 2021).

1021 Figure 2. Water-column distribution along the longitudinal transect of (a) temperature, (b)
1022 salinity, (c) A_T , (d) pH_T and (e) AOU for the cruises of 2009 (left plots) and 2016 (right plots).
1023 The vertical white lines show the limits between basins. Figure produced with Ocean Data
1024 View (Schlitzer, 2021).

1025 Figure 3. Water-column distribution along the longitudinal transect of (a) C_T , (b) C_{ant} and (c)
1026 C_{nat} for the cruises of 2009 (left plots) and 2016 (right plots). The vertical white lines show the
1027 limits between basins. Figure produced with Ocean Data View (Schlitzer, 2021).

1028 Figure 4. Temporal distribution (2009-2019) of the average temperature and salinity in each of
1029 the layers considered for the Irminger (left plot column), Iceland (central plot column) and
1030 Rockall basins (right plot column). The average values were calculated for each cruise and
1031 layer and represented with coloured points together with their respective error bars at the time of
1032 each cruise (the method used for calculations was described in section 3.2). In the Irminger
1033 plots, the empty points represent the average values for 2019 calculated with the measured
1034 data available in the easternmost part of the basin (sampled part during this cruise), while the
1035 coloured points for 2019 represent the average values corrected with A25-OVIDE-2018 data.
1036 The interannual trends were given by linear regression of the average values, with the values
1037 of the slope, the standard error of estimate and the r^2 presented in Table 2.

1038 Figure 5. Temporal distribution (2009-2019) of the average C_T , C_{ant} and C_{nat} in each of the
1039 layers considered for the Irminger (left plot column), Iceland (central plot column) and Rockall
1040 basins (right plot column). The average values were calculated for each cruise and layer and
1041 represented with coloured points together with their respective error bars at the time of each
1042 cruise (the method used for calculations was described in section 3.2). In the Irminger plots,
1043 the empty points represent the average values for 2019 calculated with the measured data
1044 available in the easternmost part of the basin (sampled part during this cruise), while the
1045 coloured points for 2019 represent the average values corrected with A25-OVIDE-2018 data.



1046 The interannual trends were given by linear regression of the average values, with the values
1047 of the slope, the standard error of estimate and the r^2 presented in Table 2.

1048 Figure 6. Temporal distribution (2009-2019) of the average pH_T (in situ temperature) in each
1049 of the layers considered for the Irminger (left plot column), Iceland (central plot column) and
1050 Rockall basins (right plot column). The average values were calculated for each cruise and
1051 layer and represented with coloured points together with their respective error bars at the time
1052 of each cruise (the method used for calculations was described in section 3.2). In the Irminger
1053 plots, the empty points represent the average values for 2019 calculated with the measured
1054 data available in the easternmost part of the basin (sampled part during this cruise), while the
1055 coloured points for 2019 represent the average values corrected with A25-OVIDE-2018 data.
1056 The interannual trend were given by linear regression of the average values, with the values of
1057 the slope, the standard error of estimate and the r^2 presented in Table 2.

1058 Figure 7. Temporal distribution (2009-2019) of the average Ω_{Ca} and Ω_{Arag} in each of the
1059 layers considered for the Irminger (left plot column), Iceland (central plot column) and Rockall
1060 basins (right plot column). The average values were calculated for each cruise and layer and
1061 represented with coloured points together with their respective error bars at the time of each
1062 cruise (the method used for calculations was described in section 3.2). In the Irminger plots,
1063 the empty points represent the average values for 2019 calculated with the measured data
1064 available in the easternmost part of the basin (sampled part during this cruise), while the
1065 coloured points for 2019 represent the average values corrected with A25-OVIDE-2018 data.
1066 The interannual trends were given by linear regression of the average values, with the values
1067 of the slope, the standard error of estimate and the r^2 presented in Table 2.

1068 Legend for Tables

1069 Table 1. Metadata list of hydrographic cruises.

1070 Table 2. Interannual trends of temperature, salinity, C_T , C_{ant} , C_{nat} , pH_T , Ω_{Ca} and Ω_{Arag} in each
1071 of the layers and basins. The ratios of change were based on linear regressions applied to the
1072 average values (as represented in Figures 4-7) and presented together with its Standard error
1073 of estimate. The correlation coefficients r^2 and p-values were also provided. Values in bold
1074 denote trends statistically significant at the 95% level of confidence.

1075 Table 3. Temporal changes in pH_T (in 10^{-3} units yr^{-1}) explained by fluctuations in temperature
1076 $\left(\frac{\partial pH_T}{\partial T} \frac{\partial T}{dt}\right)$, salinity $\left(\frac{\partial pH_T}{\partial S} \frac{\partial S}{dt}\right)$, A_T $\left(\frac{\partial pH_T}{\partial A_T} \frac{\partial NA_T}{dt}\right)$, and C_T $\left(\frac{\partial pH_T}{\partial C_T} \frac{\partial NC_T}{dt}\right)$ in each of the layers
1077 considered for the Irminger, Iceland and Rockall basins during the period 2009-2019. The sum
1078 of changes explained by the individual drivers represents the calculated interannual pH_T
1079 change $\left(\frac{dpH_T}{dt} \text{ calculated}\right)$, as detailed in section 2.2.5. The observed interannual pH_T trends
1080 $\left(\frac{dpH_T}{dt} \text{ observed}\right)$, shown in Figure 7 and provided in Table 2, were also added to the table for
1081 comparison.

1082 Table 4. Temporal changes in Ω_{Ca} and Ω_{Arag} (in 10^{-3} units yr^{-1}) explained by fluctuations in
1083 temperature $\left(\frac{\partial \Omega}{\partial T} \frac{\partial T}{dt}\right)$, salinity $\left(\frac{\partial \Omega}{\partial S} \frac{\partial S}{dt}\right)$, A_T $\left(\frac{\partial \Omega}{\partial A_T} \frac{\partial NA_T}{dt}\right)$, and C_T $\left(\frac{\partial \Omega}{\partial C_T} \frac{\partial NC_T}{dt}\right)$ in each of the layers
1084 considered for the Irminger, Iceland and Rockall basins during the period 2009-2019. The sum

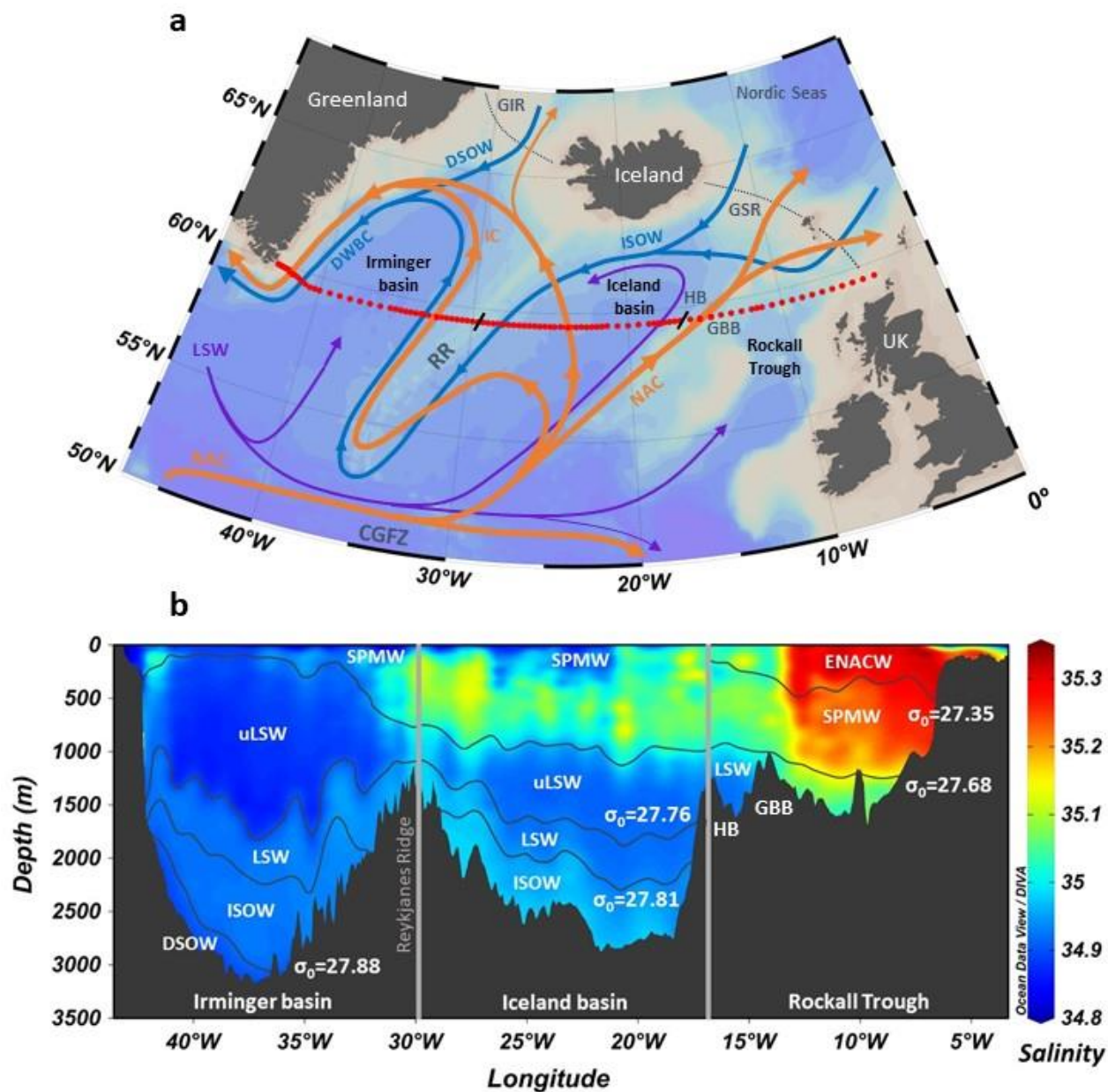


1085 of changes explained by the individual drivers represents the calculated interannual Ω change
1086 $\left(\frac{d\Omega}{dt} \text{ calculated}\right)$, as detailed in section 2.2.6. The observed interannual Ω trends
1087 $\left(\frac{d\Omega}{dt} \text{ observed}\right)$, shown in Figure 6 and provided in Table 2, were also added to the table for
1088 comparison.



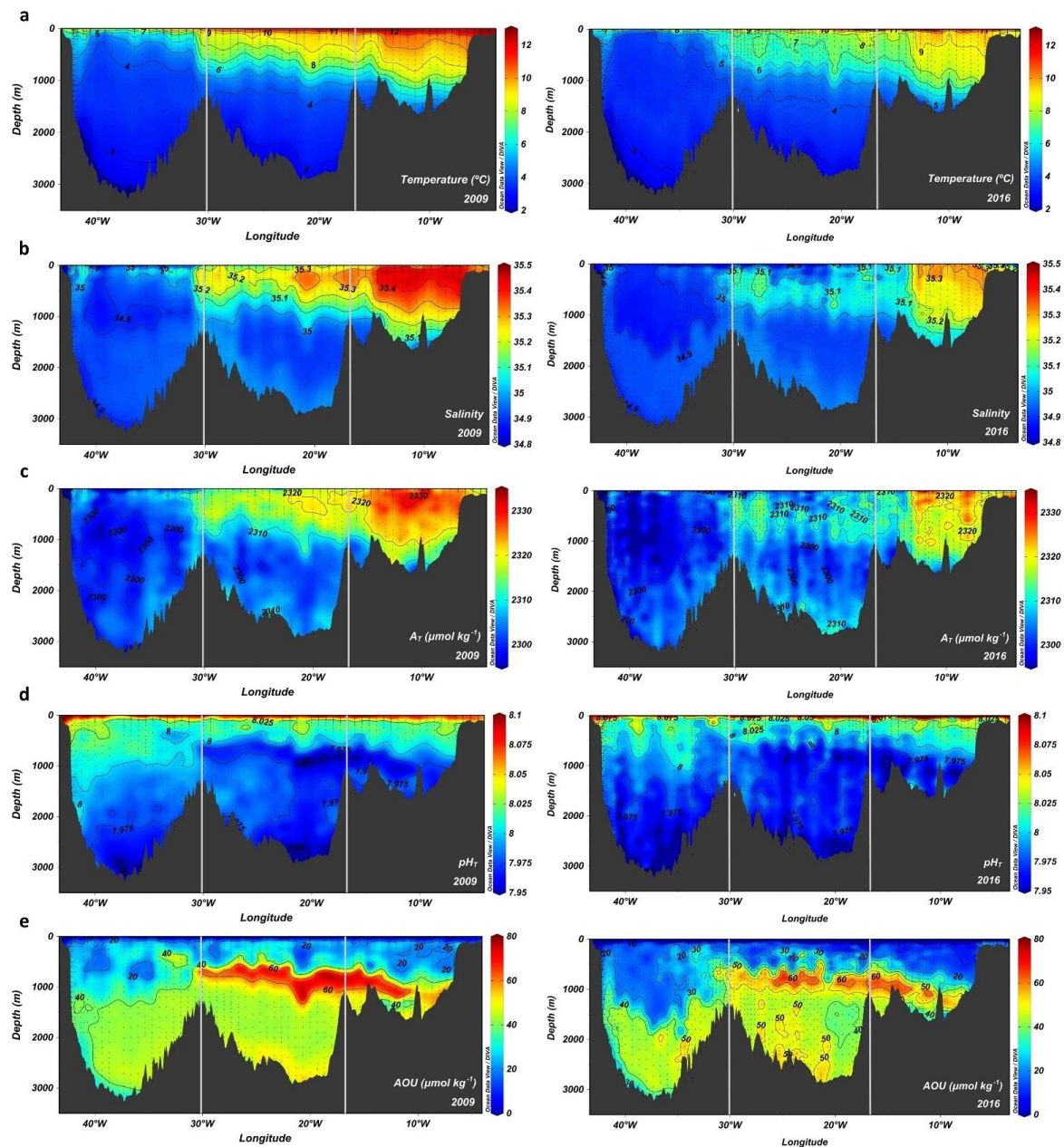
1089 **Figures**

1090 Fig. 1





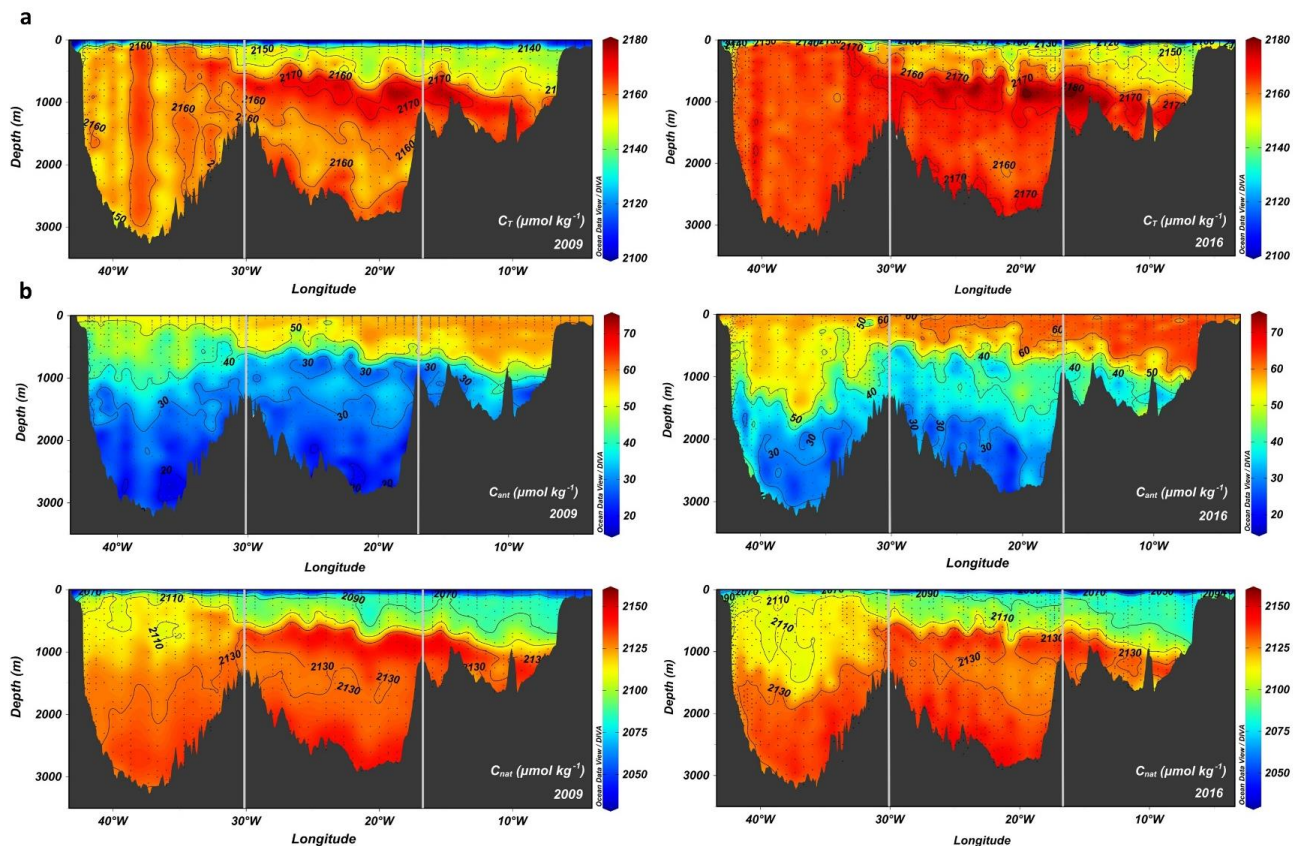
1091 Fig. 2





1092 Fig. 3

1093



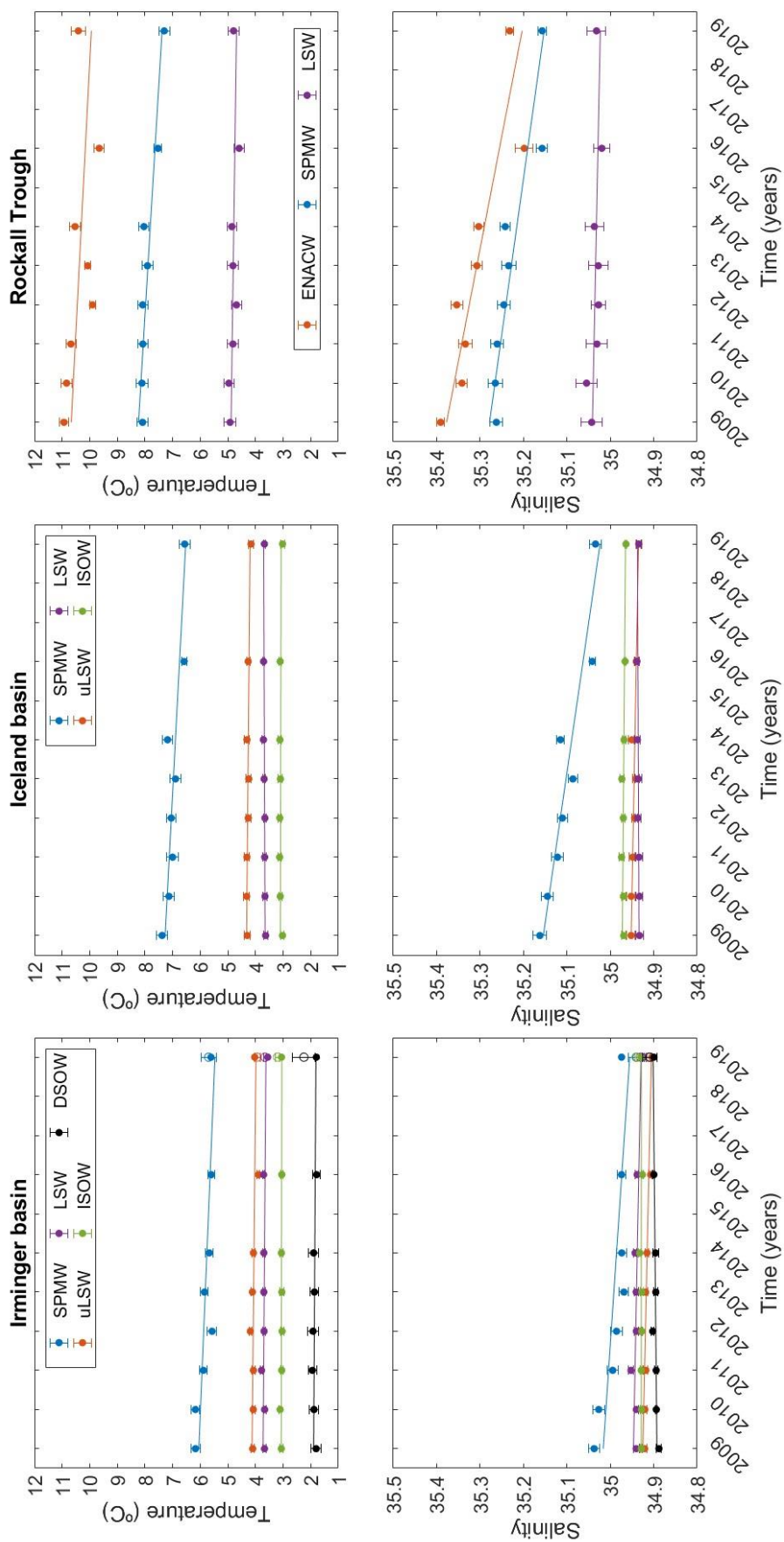


Fig. 4

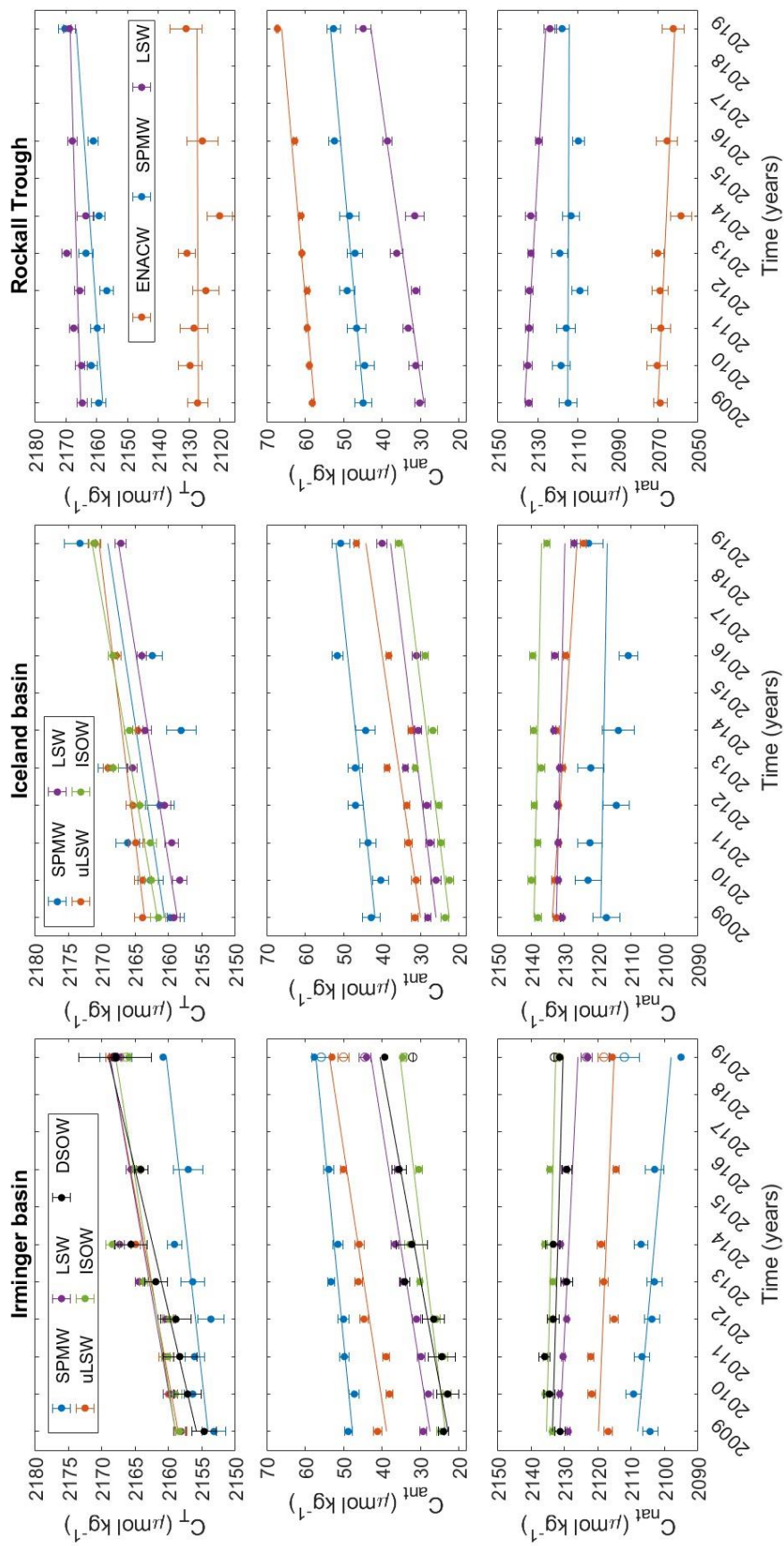


Fig. 5

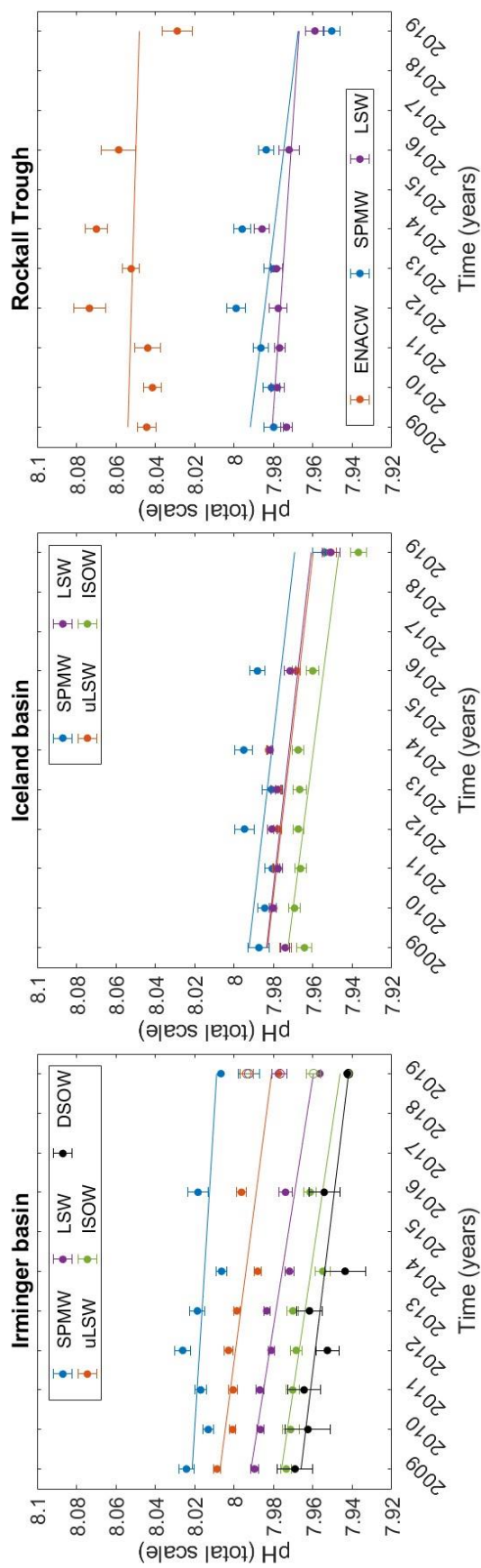


Fig. 6

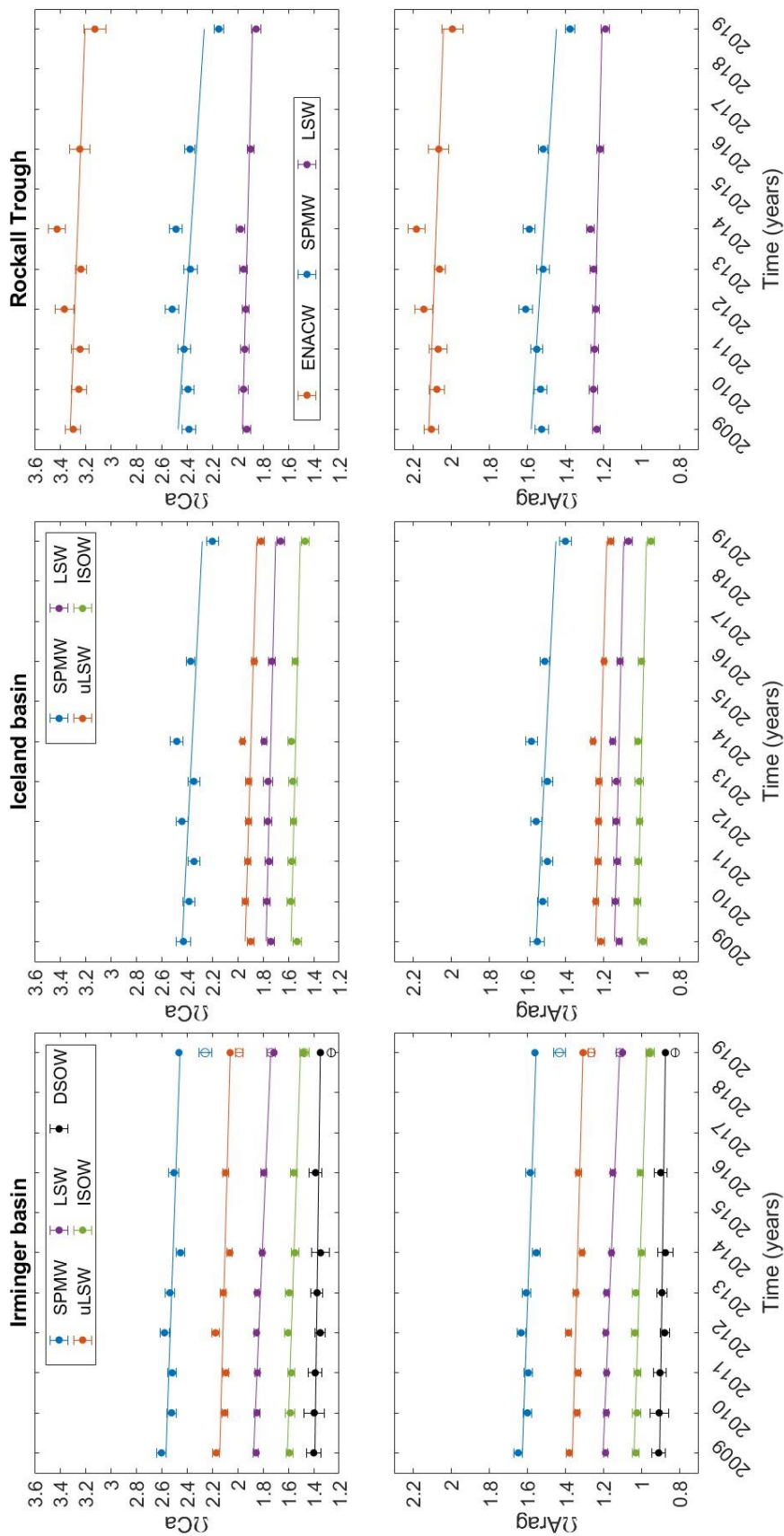


Fig. 7



Table 1

Year	Cruise ID	Date	Research Vessel (R/V)	Chief Scientist
2009	A128	Aug 15-Sept 27	Akademik Ioffe	A. Sokov
2010	A131	Sep 2-Sep 27	Akademik Ioffe	A. Sokov
2011	SV33	Sep 9-Sep 28	Akademik Sergey Vavilov	A. Sokov
2012	A138	May 25-Jul 1	Akademik Ioffe	S. Gladyshev
2013	A141	Jun 26-Jul 23	Akademik Ioffe	S. Gladyshev
2014	A144	Jun 27-Jul 20	Akademik Ioffe	S. Gladyshev
2016	A151	Jun 3-Jul 13	Akademik Ioffe	S. Gladyshev
2019	AMK77	Aug 8-Sep 10	Akademik Mstislav Keldysh	S. Gladyshev



Table 2

Basin	Layer	Temperature	Salinity	C_T	C_{ant}	C_{nut}	ph_T	Ω_{ca}	Ω_{Arag}
		ratio (°C.yr ⁻¹) r^2 p-value	ratio (psu.yr ⁻¹) r^2 p-value	ratio (μmol.kg ⁻¹ .yr ⁻¹) r^2 p-value	ratio (μmol.kg ⁻¹ .yr ⁻¹) r^2 p-value	ratio (μmol.kg ⁻¹ .yr ⁻¹) r^2 p-value	ratio (10 ⁻⁵ units.yr ⁻¹) r^2 p-value	ratio (units.yr ⁻¹) r^2 p-value	ratio (units.yr ⁻¹) r^2 p-value
Irminger	SPMW	-0.058 ± 0.024 0.60 0.02	-0.006 ± 0.003 0.59 0.03	0.62 ± 0.23 0.66 0.02	0.95 ± 0.17 0.89 <0.01	-1.00 ± 0.42 0.60 0.02	-1.25 ± 0.93 0.32 0.14	-0.011 ± 0.006 0.50 0.05	0.007 ± 0.003 0.53 0.04
	uLSW	-0.014 ± 0.011 0.30 0.16	-0.002 ± 0.001 0.59 0.03	1.02 ± 0.18 0.89 <0.01	1.48 ± 0.29 0.87 <0.01	-0.47 ± 0.38 0.28 0.18	0.69 ± 0.79 <0.01	-0.008 ± 0.005 0.40 0.09	-0.006 ± 0.003 0.44 0.08
	LSW	-0.010 ± 0.008 0.31 0.15	-0.002 ± 0.001 0.50 0.05	0.98 ± 0.26 0.78 <0.01	1.53 ± 0.23 0.92 <0.01	-0.54 ± 0.30 0.46 0.06	0.52 ± 0.91 <0.01	-0.014 ± 0.003 0.85 <0.01	-0.009 ± 0.002 0.85 <0.01
	ISOW	-0.002 ± 0.003 0.11 0.42	0.000 ± 0.000 0.00 0.99	0.90 ± 0.34 0.64 0.02	1.18 ± 0.29 0.81 <0.01	-0.27 ± 0.20 0.32 0.14	0.70 ± 0.83 <0.01	-0.010 ± 0.003 0.73 <0.01	-0.007 ± 0.002 0.74 <0.01
	DSOW	-0.008 ± 0.008 0.22 0.25	0.001 ± 0.001 0.43 0.08	1.32 ± 0.23 0.90 <0.01	1.77 ± 0.32 0.89 <0.01	-0.32 ± 0.33 0.19 0.28	0.87 ± 0.67 <0.01	-0.004 ± 0.003 0.39 0.10	-0.003 ± 0.002 0.46 0.07
Iceland	SPMW	-0.074 ± 0.022 0.74 <0.01	-0.013 ± 0.002 0.89 <0.01	0.85 ± 0.64 0.32 0.15	1.02 ± 0.31 0.74 <0.01	-0.19 ± 0.74 0.02 0.75	1.63 ± 1.63 0.34 0.13	-0.016 ± 0.010 0.37 0.11	-0.010 ± 0.007 0.39 0.10
	uLSW	-0.012 ± 0.005 0.63 0.02	-0.002 ± 0.000 0.76 <0.01	0.68 ± 0.22 0.71 <0.01	1.42 ± 0.38 0.78 <0.01	-0.74 ± 0.21 0.75 <0.01	1.01 ± 0.58 0.03	-0.009 ± 0.005 0.46 0.07	-0.006 ± 0.003 0.47 0.06
	LSW	0.005 ± 0.003 0.43 0.08	0.000 ± 0.000 0.28 0.18	0.88 ± 0.22 0.80 <0.01	1.18 ± 0.35 0.75 <0.01	-0.26 ± 0.26 0.20 0.27	1.06 ± 0.54 0.04	-0.008 ± 0.005 0.41 0.09	-0.005 ± 0.003 0.41 0.09
	ISOW	-0.003 ± 0.006 0.05 0.61	-0.001 ± 0.000 0.47 0.05	0.98 ± 0.17 0.89 <0.01	1.20 ± 0.32 0.79 <0.01	-0.23 ± 0.21 0.23 0.23	0.99 ± 0.64 <0.01	-0.007 ± 0.004 0.42 0.08	-0.005 ± 0.003 0.43 0.08
Rockall	ENACW	-0.073 ± 0.061 0.27 0.19	-0.017 ± 0.004 0.80 <0.01	0.05 ± 0.57 0.00 0.92	0.85 ± 0.11 0.94 <0.01	-0.84 ± 0.50 0.43 0.08	2.31 ± 0.02 0.77	-0.012 ± 0.013 0.18 0.30	-0.008 ± 0.008 0.19 0.28
	SPMW	-0.085 ± 0.019 0.84 <0.01	-0.013 ± 0.003 0.85 <0.01	0.86 ± 0.46 0.48 0.05	0.87 ± 0.18 0.86 <0.01	-0.07 ± 0.59 0.00 0.88	1.90 ± 0.30 0.16	-0.021 ± 0.013 0.38 0.10	-0.013 ± 0.008 0.39 0.10
	LSW	-0.020 ± 0.016 0.29 0.17	-0.002 ± 0.001 0.30 0.16	0.35 ± 0.29 0.27 0.19	1.38 ± 0.34 0.81 <0.01	-1.05 ± 0.24 0.84 <0.01	0.97 ± 0.34 0.13	-0.008 ± 0.004 0.45 0.07	-0.005 ± 0.003 0.45 0.07



Table 3

Basin	Layer	$\frac{\partial p H_T \partial T}{\partial T dt}$	$\frac{\partial p H_T \partial S}{\partial S dt}$	$\frac{\partial p H_T \partial N A_T}{\partial A_T dt}$	$\frac{\partial p H_T \partial N C_T}{\partial C_T dt}$	$\frac{d p H_T}{dt}$ (obs)	$\frac{d p H_T}{dt}$ (calculated)
Irrminger	SPMW	0.91 ± 0.38	0.05 ± 0.02	0.31 ± 0.43	-2.67 ± 0.63	-1.25 ± 0.93	-1.41 ± 0.85
	uLSW	0.22 ± 0.17	0.02 ± 0.01	-0.10 ± 0.40	-2.99 ± 0.53	-2.62 ± 0.69	-2.86 ± 0.68
	LSW	0.16 ± 0.12	0.01 ± 0.01	-0.04 ± 0.39	-2.85 ± 0.62	-3.17 ± 0.52	-2.72 ± 0.74
	ISOW	0.03 ± 0.05	0.00 ± 0.00	-0.13 ± 0.30	-2.38 ± 0.88	-2.97 ± 0.70	-2.48 ± 0.93
	DSOW	0.13 ± 0.12	-0.01 ± 0.00	-0.60 ± 0.18	-3.41 ± 0.62	-2.41 ± 0.87	-3.90 ± 0.66
Iceland	SPMW	1.15 ± 0.35	0.10 ± 0.02	0.61 ± 0.19	-4.14 ± 1.76	-2.32 ± 1.63	-2.27 ± 1.81
	uLSW	0.19 ± 0.08	0.01 ± 0.00	-0.24 ± 0.45	-2.08 ± 0.66	-2.31 ± 1.01	-2.12 ± 0.80
	LSW	-0.08 ± 0.05	0.00 ± 0.00	-0.04 ± 0.44	-2.26 ± 0.57	-2.26 ± 1.06	-2.38 ± 0.72
	ISOW	0.04 ± 0.10	0.01 ± 0.00	0.12 ± 0.40	-2.70 ± 0.43	-2.58 ± 0.99	-2.53 ± 0.60
Rockall	ENACW	1.13 ± 0.94	0.14 ± 0.04	0.73 ± 0.66	-2.25 ± 1.39	-0.58 ± 2.31	-0.25 ± 1.80
	SPMW	1.31 ± 0.29	0.10 ± 0.02	0.47 ± 0.22	-3.84 ± 1.23	-2.43 ± 1.90	-1.96 ± 1.28
	LSW	0.30 ± 0.24	0.01 ± 0.01	-0.14 ± 0.37	-0.94 ± 0.86	-1.36 ± 0.97	-0.76 ± 0.96



Table 4

Basin	Layer	$\frac{\partial \Omega}{\partial T} \frac{\partial T}{\partial t}$	$\frac{\partial \Omega}{\partial S} \frac{\partial S}{\partial t}$	$\frac{\partial \Omega}{\partial A_r} \frac{\partial N A_r}{\partial t}$	$\frac{\partial \Omega}{\partial C_r} \frac{\partial N C_r}{\partial t}$	$\frac{d\Omega}{dt} (obs)$	$\frac{d\Omega}{dt} (calculated)$	
Irminger	SPMW	Calcite	-0.57 ± 0.24	-0.43 ± 0.18	1.68 ± 2.37	-13.35 ± 3.14	-11.03 ± 5.57	-12.67 ± 3.94
		Aragonite	-0.49 ± 0.20	-0.29 ± 0.12	1.07 ± 1.50	-8.47 ± 1.99	-7.17 ± 3.46	-8.17 ± 2.50
	uLSW	Calcite	-0.17 ± 0.13	-0.12 ± 0.05	-0.46 ± 1.82	-12.61 ± 2.24	-8.28 ± 5.16	-13.36 ± 2.89
		Aragonite	-0.13 ± 0.10	-0.08 ± 0.03	-0.29 ± 1.16	-8.03 ± 1.43	-5.55 ± 3.21	-8.53 ± 1.84
	LSW	Calcite	-0.15 ± 0.11	-0.09 ± 0.05	-0.17 ± 1.55	-10.42 ± 2.27	-13.54 ± 2.88	-10.83 ± 2.75
		Aragonite	-0.11 ± 0.08	-0.06 ± 0.03	-0.11 ± 0.99	-6.69 ± 1.45	-8.65 ± 1.83	-6.97 ± 1.76
	ISOW	Calcite	-0.04 ± 0.05	0.00 ± 0.01	-0.44 ± 1.03	-7.48 ± 2.75	-10.35 ± 3.23	-7.96 ± 2.94
		Aragonite	-0.02 ± 0.04	0.00 ± 0.01	-0.29 ± 0.67	-4.84 ± 1.78	-6.66 ± 2.04	-5.15 ± 1.90
DSOW	Calcite	-0.13 ± 0.12	0.03 ± 0.02	-1.78 ± 0.52	-9.23 ± 1.68	-4.30 ± 2.76	-11.11 ± 1.77	
	Aragonite	-0.09 ± 0.09	0.02 ± 0.01	-1.16 ± 0.34	-6.01 ± 1.10	-3.02 ± 1.68	-7.24 ± 1.15	
Iceland	SPMW	Calcite	-0.88 ± 0.26	-0.86 ± 0.16	3.16 ± 1.00	-19.59 ± 8.35	-15.77 ± 10.40	-18.17 ± 8.42
		Aragonite	-0.72 ± 0.22	-0.58 ± 0.10	2.02 ± 0.64	-12.48 ± 5.32	-10.37 ± 6.55	-11.77 ± 5.37
	uLSW	Calcite	-0.17 ± 0.07	-0.09 ± 0.03	-1.02 ± 1.89	-7.98 ± 2.52	-9.18 ± 5.11	-9.26 ± 3.15
		Aragonite	-0.12 ± 0.05	-0.06 ± 0.02	-0.65 ± 1.21	-5.11 ± 1.61	-5.92 ± 3.23	-5.95 ± 2.02
	LSW	Calcite	0.08 ± 0.05	0.02 ± 0.01	-0.15 ± 1.70	-7.92 ± 2.00	-7.53 ± 4.64	-7.97 ± 2.63
		Aragonite	0.06 ± 0.03	0.01 ± 0.01	-0.09 ± 1.09	-5.10 ± 1.29	-4.83 ± 2.96	-5.12 ± 1.69
	ISOW	Calcite	-0.04 ± 0.10	-0.03 ± 0.02	0.41 ± 1.37	-8.38 ± 1.33	-7.22 ± 4.34	-8.05 ± 1.91
		Aragonite	-0.03 ± 0.07	-0.02 ± 0.01	0.27 ± 0.89	-5.43 ± 0.86	-4.72 ± 2.76	-5.22 ± 1.24
ENACW	Calcite	-0.82 ± 0.69	-1.50 ± 0.38	5.16 ± 4.63	-14.21 ± 8.78	-11.60 ± 12.67	-11.37 ± 9.95	
	Aragonite	-0.79 ± 0.66	-1.00 ± 0.25	3.29 ± 2.95	-9.06 ± 5.60	-7.66 ± 7.96	-7.57 ± 6.37	
SPMW	Calcite	-1.15 ± 0.26	-0.82 ± 0.18	2.44 ± 1.15	-18.21 ± 5.83	-20.57 ± 13.40	-17.74 ± 5.95	
	Aragonite	-0.93 ± 0.21	-0.55 ± 0.12	1.56 ± 0.74	-11.66 ± 3.73	-13.24 ± 8.47	-11.58 ± 3.81	
LSW	Calcite	-0.28 ± 0.22	-0.10 ± 0.08	-0.58 ± 1.57	-3.62 ± 3.30	-7.88 ± 4.41	-4.59 ± 3.66	
	Aragonite	-0.21 ± 0.16	-0.07 ± 0.05	-0.37 ± 1.01	-2.33 ± 2.12	-4.97 ± 2.82	-2.97 ± 2.35	



References

- Accornero, A., Manno, C., Esposito, F., & Gambi, M.C. (2003). The vertical flux of particulate matter in the polynya of Terra Nova Bay. Part II. Biological components. *Antarctic Science*, 15, 175–188. DOI: 10.1017/S0954102003001214
- Álvarez, M., Pérez, F.F., Bryden, H., & Ríos, A.F. (2004). Physical and biogeochemical transports structure in the North Atlantic subpolar gyre. *Journal of Geophysical Research: Ocean*, 109. DOI: 10.1029/2003jc002015
- Álvarez, M., Ríos, A.F., Pérez, F.F., Bryden, H.L., & Rosón, G. (2003). Transports and budgets of total inorganic carbon in the subpolar and temperate North Atlantic. *Global Biogeochemical Cycles*, 17(2), 2-1-2–21. DOI: 10.1029/2002gb001881
- Anderson, L.G. (2001). of the Surface Ocean CO₂ System in the Nordic Seas and Northern North Atlantic to Climate Change Using mixed-layer salinity and temperature Model and empirical relationships between sea surface temperature and surface water CO₂ fugacity, and between sea.
- Azetsu-Scott, K., Jones, E. P., Yashayaev, I., & Gershey, R. M. (2003). Time series study of CFC concentrations in the Labrador Sea during deep and shallow convection regimes (1991–2000). *Journal of Geophysical Research: Oceans*, 108(C11).
- Balmaseda, M.A., Smith, G.C., Haines, K., Anderson, D., Palmer, T.N., & Vidard, A. (2007). Historical reconstruction of the Atlantic Meridional Overturning Circulation from the ECMWF operational ocean reanalysis. *Geophysical Research Letters*, 34, 1–6. DOI: 10.1029/2007GL031645
- Bates, N.R., Astor, Y.M., Church, M.J., Currie, K., Dore, J.E., González-Dávila, M., Lorenzoni, L., Muller-Karger, F., Olafsson, J., & Santana-Casiano, J.M. (2014). A time-series view of changing surface ocean chemistry due to ocean uptake of anthropogenic CO₂ and ocean acidification. *Oceanography*, 27, 126–141. DOI: 10.5670/oceanog.2014.16
- Bates, N.R., Best, M.H.P., Neely, K., Garley, R., Dickson, A.G., & Johnson, R.J. (2012). Detecting anthropogenic carbon dioxide uptake and ocean acidification in the North Atlantic Ocean. *Biogeosciences*, 9, 2509–2522. DOI: 10.5194/bg-9-2509-2012
- Bathmann, U. V., Noji, T.T., & von Bodungen, B. (1991). Sedimentation of pteropods in the Norwegian Sea in autumn. *Deep Sea Research Part A. Oceanographic Research Papers*, 38, 1341–1360. DOI: 10.1016/0198-0149(91)90031-A
- Benson, B.B., & Krause, D. (1984). The concentration and isotopic fractionation of oxygen dissolved in freshwater and seawater in equilibrium with the atmosphere. *Deep Sea Research Part B. Oceanographic Literature Review*, 31, 859. DOI: 10.1016/0198-0254(84)93289-8
- Bersch, M., Yashayaev, I., & Koltermann, K. P. (2007). Recent changes of the thermohaline circulation in the subpolar North Atlantic. *Ocean Dynamics*, 57, 223-235.



Bittig, H.C., Steinhoff, T., Claustre, H., Fiedler, B., Williams, N.L., Sauzède, R., Körtzinger, A., & Gattuso, J.P. (2018). An alternative to static climatologies: Robust estimation of open ocean CO₂ variables and nutrient concentrations from T, S, and O₂ data using Bayesian neural networks. *Frontiers in Marine Science*, 5, 1–29. DOI: 10.3389/fmars.2018.00328

Böning, C.W., Scheinert, M., Dengg, J., Biastoch, A., & Funk, A. (2006). Decadal variability of subpolar gyre transport and its reverberation in the North Atlantic overturning. *Geophysical Research Letters*, 33. DOI: 10.1029/2006GL026906

Brambilla, E., & Talley, L.D. (2008). Subpolar mode water in the northeastern Atlantic: 1. Averaged properties and mean circulation. *Journal of Geophysical Research: Ocean*, 113, 1–18. DOI: 10.1029/2006JC004062

Broecker, W.S., & Peng, T.H. (1983). *Tracers in the sea*: W. S. Broecker and T. H. Peng. Eldigio Press Lamont Doherty Geological Observatory, 1982, 690 pages (300 figures and tables; 740 commented bibliographic references), US \$35.00. *Geochimica et Cosmochimica Acta*, 47, 1336. DOI: 10.1016/0016-7037(83)90075-3

Bryden, H.L., King, B.A., Mccarthy, G.D., & Mcdonagh, E.L. (2014). Impact of a 30 % reduction in Atlantic meridional overturning during 2009 – 2010 683–691. DOI: 10.5194/os-10-683-2014

Caldeira, K., & Wickett, M. (2005). Ocean model predictions of chemistry changes from carbon dioxide emissions to the atmosphere and ocean. *Journal of Geophysical Research C: Oceans*, 110, 1–12. DOI: 10.1029/2004JC002671

Caldeira, K., & Wickett, M.E. (2003). Anthropogenic carbon and ocean pH. *Nature*, 425, 365. DOI: 10.1038/425365a

Carpenter, J. H. (1965). The accuracy of the Winkler method for dissolved oxygen analysis 1. *Limnology and Oceanography*, 10(1), 135-140.

Carrit, D. E., & Carpenter, J. H. (1966). Recommendation procedure for Winkler analyses of sea water for dissolved oxygen. *Journal of Marine Research*, 24, 313-318.

Carter, B.R., Bittig, H.C., Fassbender, A.J., Sharp, J.D., Takeshita, Y., Xu, Y.Y., Álvarez, M., Wanninkhof, R., Feely, R.A., & Barbero, L. (2021). New and updated global empirical seawater property estimation routines. *Limnology and Oceanography: Methods*, 19, 785–809. DOI: 10.1002/lom3.10461

Clayton, T.D., & Byrne, R.H. (1993). Spectrophotometric seawater pH measurements: total hydrogen ion concentration scale calibration of m-cresol purple and at-sea results. *Deep Sea Research Part I: Oceanographic Research Papers*, 40, 2115–2129. DOI: 10.1016/0967-0637(93)90048-8

Collier, R., Dymond, J., Honjo, S., Manganini, S., Francois, R., & Dunbar, R. (2000). The vertical flux of biogenic and lithogenic material in the Ross Sea: Moored sediment trap



observations 1996-1998. *Deep Sea Research Part II: Topical Studies in Oceanography*, 47, 3491–3520. DOI: 10.1016/S0967-0645(00)00076-X

Corbière, A., Metzl, N., Reverdin, G., Brunet, C., & Takahashi, T. (2007). Interannual and decadal variability of the oceanic carbon sink in the North Atlantic subpolar gyre. *Tellus, Series B: Chemical and Physical Meteorology*, 59, 168–178. DOI: 10.1111/j.1600-0889.2006.00232.x

Daniault, N., Mercier, H., Lherminier, P., Sarafanov, A., Falina, A., Zunino, P., Pérez, F.F., & Ríos, A.F. (2016). The northern North Atlantic Ocean mean circulation in the early 21st century. *Progress in Oceanography*, 146, 142–158. DOI: 10.1016/j.pocean.2016.06.007

de la Paz, M., García-Ibáñez, M. I., Steinfeldt, R., Ríos, A. F., & Pérez, F. F. (2017). Ventilation versus biology: What is the controlling mechanism of nitrous oxide distribution in the North Atlantic?. *Global Biogeochemical Cycles*, 31(4), 745–760. DOI: 10.1002/2016GB005507

Dickson, A. G., & Goyet, C. (1994). *Handbook of methods for the analysis of the various parameters of the carbon dioxide system in sea water*. V. 2. United States. DOI: 10.2172/10107773

Dickson, A. G., Sabine, C. L., & Christian, J. R. (2007). *Guide to best practices for ocean CO₂ measurements*. PICES Special Publication 3, 191 pp.

Dickson, B., Yashayaev, I., Meincke, J., Turrell, B., Dye, S., & Holfort, J. (2002). Rapid freshening of the deep North Atlantic Ocean over the past four decades. *Nature*, 416(6883), 832-837. DOI: 10.1038/416832a

De Jong, M. F., & de Steur, L. (2016). Strong winter cooling over the Irminger Sea in winter 2014–2015, exceptional deep convection, and the emergence of anomalously low SST. *Geophysical Research Letters*, 43, 7106–7113. DOI: 10.1002/2016GL069596

De Jong, M. F., Van Aken, H. M., Våge, K., & Pickart, R. S. (2012). Convective mixing in the central Irminger Sea: 2002-2010. *Deep Sea Research Part I: Oceanographic Research Papers*, 63, 36–51. DOI: 10.1016/j.dsr.2012.01.003

DelValls, T. A., & Dickson, A. G. (1998). The pH of buffers based on 2-amino-2-hydroxymethyl-1,3-propanediol ('tris') in synthetic sea water. *Deep Sea Research Part I: Oceanographic Research Papers*, 45, 1541–1554. DOI: 10.1016/S0967-0637(98)00019-3

Desbruyères, D., Thierry, V., & Mercier, H. (2013). Simulated decadal variability of the meridional overturning circulation across the A25-Ovide section, 462–475. DOI: 10.1029/2012JC008342

Dickson, A. G. (1990). Standard potential of the reaction: $\text{AgCl(s)} + 1/2\text{H}_2(\text{g}) = \text{Ag(s)} + \text{HCl(aq)}$, and the standard acidity constant of the ion HSO_4^- in synthetic sea water from 273.15 to 318.15 K. *J. Chem. Thermodyn.*, 22, 113–127. DOI: 10.1016/0021-9614(90)90074-Z



Dickson, A. G., & Millero, F. J. (1987). A comparison of the equilibrium constants for the dissociation of carbonic acid in seawater media. *Deep Sea Research Part A: Oceanographic Research Papers*, 34, 1733–1743. DOI: 10.1016/0198-0149(87)90021-5

Dickson, R. R., & Brown, J. (1994). The production of North Atlantic Deep Water: Sources, rates, and pathways. *J. Geophys. Res. Ocean.*, 99, 12319–12341. DOI: 10.1029/94JC00530

Doney, S. C., Fabry, V. J., Feely, R. A., & Kleypas, J. A. (2009). Ocean Acidification: The Other CO₂ Problem. *Ann. Rev. Mar. Sci.*, 1, 169–192. DOI: 10.1146/annurev.marine.010908.163834

Eden, C., & Willebrand, J. (2001). Mechanism of interannual to decadal variability of the North Atlantic circulation. *J. Clim.*, 14, 2266–2280. DOI: 10.1175/1520-0442(2001)014<2266:MOITDV>2.0.CO;2

Ellett, D. J., Edwards, A., & Bowers, R. (1986). The hydrography of the Rockall Channel—an overview. *Proc. R. Soc. Edinburgh. Sect. B. Biol. Sci.*, 88, 61–81. DOI: 10.1017/s0269727000004474

Feely, R. A., Sabine, C. L., Lee, K., Berelson, W., Kleypas, J., Fabry, V. J., Millero, F. J. (2004). Impact of anthropogenic CO₂ on the CaCO₃ system in the oceans. *Science*, 305, 362–366. DOI: 10.1126/SCIENCE.1097329

Ferron, B., Kokoszka, F., Mercier, H., Lherminier, P. (2014). Dissipation rate estimates from microstructure and finescale internal wave observations along the A25 Greenland-Portugal OVIDE line. *J. Atmos. Ocean. Technol.*, 31, 2530–2543. DOI: 10.1175/JTECH-D-14-00036.1

Fogelqvist, E., Blindheim, J., Tanhua, T., Østerhus, S., Buch, E., & Rey, F. (2003). Greenland–Scotland overflow studied by hydro-chemical multivariate analysis. *Deep Sea Research Part I: Oceanographic Research Papers*, 50(1), 73–102.

Fontela, M., Pérez, F. F., Carracedo, L. I., Padín, X. A., Velo, A., García-Ibañez, M. I., Lherminier, P. (2020). The Northeast Atlantic is running out of excess carbonate in the horizon of cold-water corals communities. *Sci. Rep.*, 10. DOI: 10.1038/s41598-020-71793-2

Friedlingstein, P., Sullivan, M. O., Jones, M. W., Andrew, R. M., Gregor, L., Hauck, J., Quéré, C. Le, Lujikx, I. T., Olsen, A., Peters, G. P., Peters, W. (2022). *Global Carbon Budget 2022*, 4811–4900.

Fröb, F., Olsen, A., Becker, M., Chafik, L., Johannessen, T., Reverdin, G., Omar, A. (2019). Wintertime fCO₂ Variability in the Subpolar North Atlantic Since 2004. *Geophys. Res. Lett.*, 46, 1580–1590. DOI: 10.1029/2018GL080554

Fröb, F., Olsen, A., Våge, K., Moore, G. W. K., Yashayaev, I., Jeansson, E., Rajasakaren, B. (2016). Irminger Sea deep convection injects oxygen and anthropogenic carbon to the ocean interior. *Nat. Commun.*, 7. DOI: 10.1038/ncomms13244



García-Ibáñez, M. I., Bates, N. R., Bakker, D. C. E., Fontela, M., Velo, A. (2021). Cold-water corals in the Subpolar North Atlantic Ocean exposed to aragonite undersaturation if the 2 °C global warming target is not met. *Global Planetary Change*, 201. DOI: 10.1016/j.gloplacha.2021.103480

García-Ibáñez, M. I., Pardo, P. C., Carracedo, L. I., Mercier, H., Lherminier, P., Ríos, A. F., Pérez, F. F. (2015). Structure, transports and transformations of the water masses in the Atlantic Subpolar Gyre. *Progress in Oceanography*, 135, 18-36. DOI: 10.1016/j.pocean.2015.03.009

García-Ibáñez, M. I., Pérez, F. F., Lherminier, P., Zunino, P., Mercier, H., Tréguer, P. (2018). Water mass distributions and transports for the 2014 GEOVIDE cruise in the North Atlantic. *Biogeosciences*, 15, 2075-2090. DOI: 10.5194/bg-15-2075-2018

García-Ibáñez, M. I., Zunino, P., Fröb, F., Carracedo, L. I., Ríos, A. F., Mercier, H., Olsen, A., Pérez, F. F. (2016). Ocean acidification in the subpolar North Atlantic: Rates and mechanisms controlling pH changes. *Biogeosciences*, 13, 3701-3715. DOI: 10.5194/bg-13-3701-2016

Gladyshev, S. V., Gladyshev, V. S., Falina, A. S., Sarafanov, A. A. (2016a). Winter convection in the Irminger Sea in 2004–2014. *Oceanology*, 56, 326-335. DOI: 10.1134/S0001437016030073

Gladyshev, S. V., Gladyshev, V. S., Gulev, S. K., Sokov, A. V. (2016b). Anomalously deep convection in the Irminger Sea during the winter of 2014–2015. *Doklady Earth Sciences*, 469, 766-770. DOI: 10.1134/S1028334X16070229

Gladyshev, S. V., Gladyshev, V. S., Gulev, S. K., Sokov, A. V. (2016c). Anomalously deep convection in the Irminger Sea during the winter of 2014–2015. *Doklady Earth Sciences*, 469, 766-770. DOI: 10.1134/S1028334X16070229

Gladyshev, S. V., Gladyshev, V. S., Member, C., Gulev, R. A. S. S. K., Sokov, A. V. (2018). Structure and Variability of the Meridional Overturning Circulation in the North Atlantic Subpolar Gyre, 2007–2017. *Doklady Earth Sciences*, 483, 1524-1527. DOI: 10.1134/S1028334X18120024

Gladyshev, S. V., Gladyshev, V. S., Member, C., Gulev, R. A. S. S. K., Sokov, A. V. (2017). Subpolar Mode Water Classes in the Northeast Atlantic: Interannual and Long-Term Variability. *Doklady Earth Sciences*, 476, 1203-1206. DOI: 10.1134/S1028334X17100166

González-Dávila, M., Santana-Casiano, J. M., Petihakis, G., Ntoumas, M., Suárez de Tangil, M., Krasakopoulou, E. (2016). Seasonal pH variability in the Saronikos Gulf: A year-study using a new photometric pH sensor. *Journal of Marine Systems*, 162, 37-46. DOI: 10.1016/j.jmarsys.2016.03.007

González-Dávila, M., Santana-Casiano, J. M., Prêcheur-Massieu, H. (2014). New pH sensor for monitoring ocean acidification. *Sea Technology*, 55, 36-40.



González-Dávila, M., Santana-Casiano, J.M., Rueda, M.J., Llinás, O. (2010). The water column distribution of carbonate system variables at the ESTOC site from 1995 to 2004. *Biogeosciences*, 7, 3067–3081. DOI: 10.5194/bg-7-3067-2010

Gruber, N., Clement, D., Carter, B.R., Feely, R.A., van Heuven, S., Hoppema, M., Ishii, M., Key, R.M., Kozyr, A., Lauvset, S.K., Monaco, C. Lo, Mathis, J.T., Murata, A., Olsen, A., Perez, F.F., Sabine, C.L., Tanhua, T., Wanninkhof, R. (2019a). The oceanic sink for anthropogenic CO₂ from 1994 to 2007. *Science*, 363, 1193

Gruber, N., Sarmiento, J.L., Stocker, T.F. (1996). An improved method for detecting anthropogenic CO₂ in the oceans. *Global Biogeochem. Cycles*. <https://doi.org/10.1029/96GB01608>

Gualart, E.F., Fajar, N.M., Padín, X.A., Vázquez-Rodríguez, M., Calvo, E., Ríos, A.F., Hernández-Guerra, A., Pelejero, C., Pérez, F.F. (2015). Ocean acidification along the 24.5°N section in the subtropical North Atlantic. *Geophys. Res. Lett.*, 42, 450–458. <https://doi.org/10.1002/2014GL062971>

Häkkinen, S. (2002). Surface salinity variability in the northern North Atlantic during recent decades. *J. Geophys. Res. Ocean*, 107, SRF 4-1. <https://doi.org/10.1029/2001JC000812>

Häkkinen, S., Rhines, P.B. (2004). Decline of Subpolar North Atlantic Circulation during the 1990s. *Science* (80-.), 304, 555–559. <https://doi.org/10.1126/science.1094917>

Harvey, J. (1982). Theta–S relationships and water masses in the eastern North Atlantic. *Deep-Sea Res. Part a-Oceanogr. Res. Pap.*, 29 (8), 1021–1033.

Hátún, H., Sande, A.B., Drange, H., Hansen, B., Valdimarsson, H. (2005). Influence of the Atlantic subpolar gyre on the thermohaline circulation. *Science* (80-.), 309, 1841–1844. <https://doi.org/10.1126/science.1114777>

Holliday, N.P., Bersch, M., Berx, B., Chafik, L., Cunningham, S., Florindo-López, C., Hátún, H., Johns, W., Josey, S.A., Larsen, K.M.H., Mulet, S., Oltmanns, M., Reverdin, G., Rossby, T., Thierry, V., Valdimarsson, H., Yashayaev, I. (2020). Ocean circulation causes the largest freshening event for 120 years in eastern subpolar North Atlantic. *Nat. Commun.*, 11. <https://doi.org/10.1038/s41467-020-14474-y>

Holliday, P. N., Pollard, R.T., Read, J.F., Leach, H. (2000). Water mass properties and fluxes in the Rockall Trough, 1975–1998. *Deep-Sea Research Part I: Oceanographic Research Papers*. [https://doi.org/10.1016/S0967-0637\(99\)00109-0](https://doi.org/10.1016/S0967-0637(99)00109-0)

Humphreys, M. P., et al. (2016). Multidecadal accumulation of anthropogenic and remineralized dissolved inorganic carbon along the Extended Ellett Line in the northeast Atlantic Ocean. *Global Biogeochem. Cycles*. 30, 293–310, doi:10.1002/2015GB005246.

IPCC (2007). *Climate Change 2007: The Physical Science Basis*. Contribution of Working Group I to the Fourth Assessment Report of the Intergovernmental Panel on Climate Change.



IPCC (2021). *Climate Change 2021: The Physical Science Basis. Contribution of Working Group I to the Sixth Assessment Report of the Intergovernmental Panel on Climate Change.*

IPCC Working Group (2013). *Climate Change 2013: The Physical Science Basis. Working Group I Contribution to the Fifth Assessment Report of the Intergovernmental Panel on Climate Change* (Cambridge Univ. Press).

Jackson, L.C., Biastoch, A., Buckley, M.W., Desbruyères, D. G., Frajka-Williams, E., Moat, B., and Robson, J. (2022). The evolution of the North Atlantic Meridional Overturning Circulation since 1980. *Nat. Rev. Earth Environ.* 3, 241–254. <https://doi.org/10.1038/s43017-022-00263-2>

Jiang, L.Q., Feely, R.A., Carter, B.R., Greeley, D.J., Gledhill, D.K., Arzayus, K.M. (2015). Climatological distribution of aragonite saturation state in the global oceans. *Global Biogeochem. Cycles*, 29, 1656–1673. <https://doi.org/10.1002/2015GB005198>

Johnson, K.M., Wills, K.D., Butler, D.B., Johnson, W.K., Wong, C.S. (1993). Coulometric total carbon dioxide analysis for marine studies: maximizing the performance of an automated gas extraction system and coulometric detector. *Mar. Chem.*, 44, 167–187. [https://doi.org/10.1016/0304-4203\(93\)90201-X](https://doi.org/10.1016/0304-4203(93)90201-X)

Josey, S.A., Hirschi, J.J.M., Sinha, B., Ducez, A., Grist, J.P., Marsh, R. (2018). The recent Atlantic cold anomaly: Causes, consequences, and related phenomena. *Ann. Rev. Mar. Sci.*, 10, 475–501. <https://doi.org/10.1146/annurev-marine-121916-063102>

Khatiwal, S., Tanhua, T., Mikaloff Fletcher, S., Gerber, M., Doney, S.C., Graven, H.D., Gruber, N., McKinley, G.A., Murata, A., Rios, A.F., Sabine, C.L. (2013). Global ocean storage of anthropogenic carbon. *Biogeosciences*, 10, 2169–2191. <https://doi.org/10.5194/bg-10-2169-2013>

Kieke, D., Rhein, M., Stramma, L., Smethie, W. M., Bullister, J. L., & LeBel, D. A. (2007). Changes in the pool of Labrador Sea Water in the subpolar North Atlantic. *Geophysical Research Letters*, 34(6).

Knight, J.R., Folland, C.K., Scaife, A.A. (2006). Climate impacts of the Atlantic multidecadal oscillation. *Geophys. Res. Lett.*, 33, 2–5. <https://doi.org/10.1029/2006GL026242>

Langdon, C., Takahashi, T., Sweeney, C., Chipman, D., Atkinson, J. (2000). Rate of an experimental coral reef responds to manipulations in the concentrations of both CaCO₃. *Global Biogeochem. Cycles*, 14, 639–654.

Lazier, J., Hendry, R., Clarke, A., Yashayaev, I., Rhines, P. (2002). Convection and restratification in the Labrador Sea, 1990–2000. *Deep Sea Res. Part I Oceanogr. Res. Pap.*, 49, 1819–1835. [https://doi.org/10.1016/S0967-0637\(02\)00064-X](https://doi.org/10.1016/S0967-0637(02)00064-X)

Lee, K., Kim, T.W., Byrne, R.H., Millero, F.J., Feely, R.A., Liu, Y.M. (2010). The universal ratio of boron to chlorinity for the North Pacific and North Atlantic oceans. *Geochim. Cosmochim. Acta*, 74, 1801–1811. <https://doi.org/10.1016/j.gca.2009.12.027>



Leseurre, C., Lo Monaco, C., Reverdin, G., Metzl, N., Fin, J., Olafsdottir, S., Racapé, V. (2020). Ocean carbonate system variability in the North Atlantic Subpolar surface water (1993–2017). *Biogeosciences*, 17, 2553–2577. <https://doi.org/10.5194/bg-17-2553-2020>

Lewis, E., Wallace, D. (1998). Program Developed for CO₂ System Calculations ORNL/CDIAC-105, Carbon Dioxide Information Analysis Centre.

Lherminier, P., Mercier, H., Huck, T., Gourcuff, C., Perez, F. F., Morin, P., ... & Falina, A. (2010). The Atlantic Meridional Overturning Circulation and the subpolar gyre observed at the A25-OVIDE section in June 2002 and 2004. *Deep Sea Research Part I: Oceanographic Research Papers*, 57(11), 1374-1391.

Lueker, T.J., Dickson, A.G., Keeling, C.D. (2000). Ocean pCO₂ calculated from dissolved inorganic carbon, alkalinity, and equations for K₁ and K₂: Validation based on laboratory measurements of CO₂ in gas and seawater at equilibrium. *Mar. Chem.*, 70, 105–119. [https://doi.org/10.1016/S0304-4203\(00\)00022-0](https://doi.org/10.1016/S0304-4203(00)00022-0)

Marsh, R., de Cuevas, B.A., Coward, A.C., Bryden, H.L., Álvarez, M. (2005). Thermohaline circulation at three key sections in the North Atlantic over 1985–2002. *Geophys. Res. Lett.*, 32, 1–4. <https://doi.org/10.1029/2004GL022281>

Matear, R.J., Lenton, A. (2014). Quantifying the impact of ocean acidification on our future climate. *Biogeosciences*, 11, 3965–3983. <https://doi.org/10.5194/bg-11-3965-2014>

Maier-Reimer, E., & Hasselmann, K. (1987). Transport and storage of CO₂ in the ocean: an inorganic ocean-circulation carbon cycle model. *Climate dynamics*, 2, 63-90.

Maier, C., Hegeman, J., Weinbauer, M. G., & Gattuso, J. P. (2009). Calcification of the cold-water coral *Lophelia pertusa*, under ambient and reduced pH. *Biogeosciences*, 6(8), 1671-1680. <https://doi.org/10.5194/bg-6-1671-2009>

Mauritzen, C., Häkkinen, S. (1999). On the relationship between dense water formation and the “Meridional Overturning Cell” in the North Atlantic Ocean. *Deep. Res. Part I Oceanogr. Res. Pap.*, 46, 877–894. [https://doi.org/10.1016/S0967-0637\(98\)00094-6](https://doi.org/10.1016/S0967-0637(98)00094-6)

McDonagh, E.L., King, B.A., Bryden, H.L., Courtois, P., Szuts, Z., Baringer, M., Cunningham, S.A., Atkinson, C., McCarthy, G. (2015). Continuous estimate of Atlantic oceanic freshwater flux at 26.5°N. *Journal of Climate*, 28, 8888–8906. <https://doi.org/10.1175/JCLI-D-14-00519.1>

McGrath, T., Kivimäe, C., McGovern, E., Cave, R.R., Joyce, E. (2013). Winter measurements of oceanic biogeochemical parameters in the Rockall Trough (2009-2012). *Earth System Science Data*, 5, 375–383. <https://doi.org/10.5194/essd-5-375-2013>

McGrath, T., Kivimäe, C., Tanhua, T., Cave, R.R., McGovern, E. (2012a). Inorganic carbon and pH levels in the Rockall Trough 1991-2010. *Deep Sea Research Part I: Oceanographic Research Papers*, 68, 79–91. <https://doi.org/10.1016/j.dsr.2012.05.011>



McGrath, T., Nolan, G., McGovern, E. (2012b). Chemical characteristics of water masses in the Rockall Trough. *Deep Sea Research Part I: Oceanographic Research Papers*, 61, 57–73. <https://doi.org/10.1016/j.dsr.2011.11.007>

McCartney, M. S., & Talley, L. D. (1982). The subpolar mode water of the North Atlantic Ocean. *Journal of Physical Oceanography*, 12(11), 1169–1188.

Mercier, H., Lherminier, P., Sarafanov, A., Gaillard, F., Daniault, N., Desbruyères, D., Falina, A., Ferron, B., Gourcuff, C., Huck, T., Thierry, V. (2015). Variability of the meridional overturning circulation at the Greenland – Portugal OVIDE section from 1993 to 2010. *Progress in Oceanography*, 132, 250–261. <https://doi.org/10.1016/j.pocean.2013.11.001>

Messias, M.J., Watson, A.J., Johannessen, T., Oliver, K.I.C., Olsson, K.A., Fogelqvist, E., Olafsson, J., Bacon, S., Balle, J., Bergman, N., Budéus, G., Danielsen, M., Gascard, J.C., Jeansson, E., Olafsdottir, S.R., Simonsen, K., Tanhua, T., Van Scoy, K., Ledwell, J.R. (2008). The Greenland Sea tracer experiment 1996–2002: Horizontal mixing and transport of Greenland Sea Intermediate Water. *Progress in Oceanography*, 78, 85–105. <https://doi.org/10.1016/J.POCEAN.2007.06.005>

Millero, F.J., Zhang, J., Lee, K., Campbell, D.M. (1993). Titration alkalinity of seawater. 44, 153–165.

Mintrop, L., Pérez, F.F., González-Dávila, M., Santana-Casiano, J.M., Körtzinger, A. (2000). Alkalinity determination by potentiometry: Intercalibration using three different methods. *Ciencias Marinas*, 26, 23–37. <https://doi.org/10.7773/cm.v26i1.573>

Mucci, A. (1983). The solubility of calcite and aragonite in seawater at various salinities, temperatures, and one atmosphere total pressure. *American Journal of Science*, 283(7), 780–799.

Olafsson, J., Olafsdottir, S.R., Benoit-Cattin, A., Danielsen, M., Arnarson, T.S., Takahashi, T. (2009). Rate of Iceland Sea acidification from time series measurements. *Biogeosciences*, 6, 2661–2668. <https://doi.org/10.5194/bg-6-2661-2009>

Olafsson, J., Olafsdottir, S.R., Benoit-Cattin, A., Takahashi, T. (2010). The Irminger Sea and the Iceland Sea time series measurements of seawater carbon and nutrient chemistry 1983–2008. *Earth System Science Data*, 2, 99–104. <https://doi.org/10.5194/essd-2-99-2010>

Orr, J. C. (2011). Recent and future changes in ocean carbonate chemistry. In *Ocean Acidification* (Vol. 1), Oxford University Press, 41–66.

Orr, J.C., Epitalon, J.-M., Dickson, A. G., Gattuso, J.-P., (2018). Routine uncertainty propagation for the marine carbon dioxide system. *Marine Chemistry* 207, 84–107. <https://doi.org/10.1016/j.marchem.2018.10.006>

Orr, J.C., Fabry, V.J., Aumont, O., Bopp, L., Doney, S.C., Feely, R.A., Gnanadesikan, A., Gruber, N., Ishida, A., Joos, F., Key, R.M., Lindsay, K., Maier-Reimer, E., Matear, R., Monfray, P., Mouchet, A., Najjar, R.G., Plattner, G.K., Rodgers, K.B., Sabine, C.L., Sarmiento, J.L.,



Schlitzer, R., Slater, R.D., Totterdell, I.J., Weirig, M.F., Yamanaka, Y., Yool, A. (2005). Anthropogenic ocean acidification over the twenty-first century and its impact on calcifying organisms. *Nature*, 437, 681–686. [<https://doi.org/10.1038/nature>]

Pascale, L., Perez, F. F., Branellec, P., Mercier, H., Velo, A., Messias, M. J., Castrillejo, M., Reverdin, G., Fontela, M., Baurand, F. (2022). GO-SHIP A25 - OVIDE 2018 Cruise data. SEANOE. <https://doi.org/10.17882/87394>

Pérez, F.F., Fontela, M., García-Ibáñez, M.I., Mercier, H., Velo, A., Lherminier, P., Zunino, P., De La Paz, M., Alonso-Pérez, F., Guallart, E.F., Padin, X.A. (2018). Meridional overturning circulation conveys fast acidification to the deep Atlantic Ocean. *Nature*, 554, 515–518. <https://doi.org/10.1038/nature25493>

Pérez, F.F., Fraga, F. (1987). Association constant of fluoride and hydrogen ions in seawater. *Marine Chemistry*, 21, 161–168. [https://doi.org/10.1016/0304-4203\(87\)90036-3](https://doi.org/10.1016/0304-4203(87)90036-3)

Pérez, F.F., Mercier, H., Vázquez-Rodríguez, M., Lherminier, P., Velo, A., Pardo, P.C., Rosón, G., Ríos, A.F. (2013). Atlantic Ocean CO₂ uptake reduced by weakening of the meridional overturning circulation. *Nature Geoscience*, 6, 146–152. <https://doi.org/10.1038/ngeo1680>

Pérez, F.F., Olafsson, J., Ólafsdóttir, S.R., Fontela, M., Takahashi, T. (2021). Contrasting drivers and trends of ocean acidification in the subarctic Atlantic. *Scientific Reports*, 11, 1–16. <https://doi.org/10.1038/s41598-021-93324-3>

Pérez, F.F., Vázquez-Rodríguez, M., Louarn, E., Padín, X.A., Mercier, H., Ríos, A.F. (2008). Temporal variability of the anthropogenic CO₂ storage in the Irminger Sea. *Biogeosciences*, 5, 1669–1679. <https://doi.org/10.5194/bg-5-1669-2008>

Pérez, F.F., Vázquez-Rodríguez, M., Mercier, H., Velo, A., Lherminier, P., Ríos, A.F. (2010). Trends of anthropogenic CO₂ storage in North Atlantic water masses. *Biogeosciences*, 7, 1789–1807. <https://doi.org/10.5194/bg-7-1789-2010>

Perez, F. F., Becker, M., Goris, N., Gehlen, M., Lopez-Mozos, M., Tjiputra, J., Olsen, A., Müller, J. D., Huertas, I. E., Chau, T. T. T., Cainzos, V., Velo, A., Benard, G., Hauck, J., Gruber, N., Wanninkhof, R. (2024). An assessment of CO₂ storage and sea-air fluxes for the Atlantic Ocean and Mediterranean Sea between 1985 and 2018. *Global Biogeochemical Cycles*, 38, e2023GB007862. <https://doi.org/10.1029/2023GB007862>

Pickart, R.S., Spall, M.A., Ribergaard, M.H., Moore, G.W.K., Milliff, R.F. (2003). Deep convection in the Irminger Sea forced by the Greenland tip jet. *Nature*, 424, 152–156. <https://doi.org/10.1038/nature01729>

Piron, A., Thierry, V., Mercier, H., Caniaux, G. (2017). Gyre-scale deep convection in the subpolar North Atlantic Ocean during winter 2014–2015. *Geophysical Research Letters*, 44, 1439–1447. <https://doi.org/10.1002/2016GL071895>

Pollard, R.T., Griffiths, M.J., Cunningham, S.A., Read, J.F., Pérez, F.F., Ríos, A.F. (1996). Vivaldi 1991 - A study of the formation, circulation, and ventilation of Eastern North Atlantic



Central Water. *Progress in Oceanography*, 37, 167–172. [https://doi.org/10.1016/S0079-6611\(96\)00008-0](https://doi.org/10.1016/S0079-6611(96)00008-0)

Portner, H.O., Langenbuch, M., & Reipschläger, A. (2004). Biological Impact of Elevated Ocean CO₂ Concentrations: Lessons from Animal Physiology and Earth History. *Journal of Oceanography*, 60, 705–718.

Pörtner, H. O., et al. (2019). IPCC Special Report on the Ocean and Cryosphere in a Changing Climate. Wiley IPCC Intergovernmental Panel on Climate Change.

Raven, J., Caldeira, K., Elderfield, H., Hoegh-Guldberg, O., Liss, P., Riebesell, U., Shepherd, J., Turley, C., & Watson, A. (2005). Ocean acidification due to increasing. *Coral Reefs*, 12/05, 68.

Read, J.F. (2000). CONVEX-91: Water masses and circulation of the Northeast Atlantic subpolar gyre. *Progress in Oceanography*, 48, 461–510. [https://doi.org/10.1016/S0079-6611\(01\)00011-8](https://doi.org/10.1016/S0079-6611(01)00011-8)

Riebesell, U., Zondervan, I., Rost, B., Tortell, P.D., Zeebe, R.E., Morel, F.M.M. (2000). Reduced calcification of marine plankton in response to increased atmospheric CO₂. *Nature*, 407, 364–366. <https://doi.org/10.1038/35030078>

Ríos, A.F., Resplandy, L., García-Ibáñez, M.I., Fajar, N.M., Velo, A., Padin, X.A., Wanninkhof, R., Steinfeldt, R., Rosón, G., Pérez, F.F., Morel, F.M.M. (2015). Decadal acidification in the water masses of the Atlantic Ocean. *Proceedings of the National Academy of Sciences, U.S.A.*, 112, 9950–9955. <https://doi.org/10.1073/pnas.1504613112>

Roberts, J.M., Wheeler, A.J., Freiwald, A., Cairns, S. (2009). *Cold-Water Corals: The Biology and Geology of Deep-Sea Coral Habitats*. Cambridge University Press. <https://doi.org/10.1017/CBO9780511581588>.

Robson, J., Hodson, D., Hawkins, E., Sutton, R. (2014). Atlantic overturning in decline? *Nature Geoscience*, 7, 2–3. <https://doi.org/10.1038/ngeo2050>

Robson, J., Ortega, P., Sutton, R. (2016). A reversal of climatic trends in the North Atlantic since 2005. *Nature Geoscience*, 9, 513–517. <https://doi.org/10.1038/ngeo2727>

Rodgers, K.B., Key, R.M., Gnanadesikan, A., Sarmiento, J.L., Aumont, O., Bopp, L., Doney, S.C., Dunne, J.R., Glover, D.M., Ishida, A., Ishii, M., Jacobson, A.R., Monaco, C. Lo, Maier-Reimer, E., Mercier, H., Metzl, N., Pérez, F.F., Rios, A.F., Wanninkhof, R., Wetzel, P., Winn, C.D., Yamanaka, Y. (2009). Using altimetry to help explain patchy changes in hydrographic carbon measurements. *Journal of Geophysical Research: Ocean*, 114, 1–20. <https://doi.org/10.1029/2008JC005183>

Sabine, C.L., Feely, R.A., Gruber, N., Key, R.M., Lee, K., Bullister, J.L., Wanninkhof, R., Wong, C.S., Wallace, D.W.R., Tilbrook, B., Millero, F.J., Peng, T.H., Kozyr, A., Ono, T., Rios, A.F. (2004a). The oceanic sink for anthropogenic CO₂. *Science*, 305, 367–371. <https://doi.org/10.1126/science.1097403>



Sabine, C.L., Feely, R.A., Gruber, N., Key, R.M., Lee, K., Bullister, J.L., Wanninkhof, R., Wong, C.S., Wallace, D.W.R., Tilbrook, B., Millero, F.J., Peng, T.H., Kozyr, A., Ono, T., Rios, A.F. (2004b). The oceanic sink for anthropogenic CO₂. *Science*, 305, 367–371. https://doi.org/10.1126/SCIENCE.1097403/SUPPL_FILE/SABINE.SOM.PDF

Santana-Casiano, J. M., González-Dávila, M., and Curbelo-Hernández, D. (2023). Surface-to-bottom data of total alkalinity, total inorganic carbon, pH and dissolved oxygen in the subpolar North Atlantic along the CLIVAR 59.5N hydrographic section during 2009-2019. [Data set]. Zenodo. <https://doi.org/10.5281/zenodo.10276222>

Santana-Casiano, J.M., González-Dávila, M., Rueda, M.-J., Llinás, O., González-Dávila, E.-F. (2007). The interannual variability of oceanic CO₂ parameters in the northeast Atlantic subtropical gyre at the ESTOC site. *Global Biogeochemical Cycles*, 21. <https://doi.org/10.1029/2006GB002788>

Sarafanov, A., Falina, A., Mercier, H., Sokov, A., Lherminier, P., Gourcuff, C., Gladyshev, S., Gaillard, F., and Daniault, N. (2012). Mean full-depth summer circulation and transports at the northern periphery of the Atlantic Ocean in the 2000s. *Journal of Geophysical Research: Oceans*, 117(C1).

Sarafanov, A., Falina, A., Sokov, A., Zapotylo, V., Gladyshev, S. (2018). Ship-Based Monitoring of the Northern North Atlantic Ocean by the Shirshov Institute of Oceanology. The Main Results. In: Velarde, M., Tarakanov, R., Marchenko, A. (eds) *The Ocean in Motion*. Springer Oceanography. Springer, Cham. https://doi.org/10.1007/978-3-319-71934-4_25

Sarafanov, A., Mercier, H., Falina, A., and Sokov, A. (2010). Cessation and partial reversal of deep water freshening in the northern North Atlantic: observation-based estimates and attribution. *Tellus A: Dynamic Meteorology and Oceanography*, 62:1, 80-90. <https://doi.org/10.1111/j.1600-0870.2009.00418.x>

Sarmiento, J.L., Orr, J.C., Siegenthaler, U. (1992). A perturbation simulation of CO₂ uptake in an ocean general circulation model. *Journal of Geophysical Research: Ocean*, 97, 3621–3645. <https://doi.org/10.1029/91JC02849>

Saunders, P. M., (2001). Chapter 5.6 The dense northern overflows. *Int. Geophys.*, 77, 401–417. [https://doi.org/10.1016/S0074-6142\(01\)80131-5](https://doi.org/10.1016/S0074-6142(01)80131-5)

Sauzède, R., Bittig, H.C., Claustre, H., de Fommervault, O.P., Gattuso, J.P., Legendre, L., Johnson, K.S. (2017). Estimates of water-column nutrient concentrations and carbonate system parameters in the global ocean: A novel approach based on neural networks. *Frontiers in Marine Science*, 4, 1–17. <https://doi.org/10.3389/fmars.2017.00128>

Schlitzer, R. (2021). Ocean Data View. Available at: <https://odv.awi.de>.

Schmitz Jr, W. J., & McCartney, M. S. (1993). On the north Atlantic circulation. *Reviews of Geophysics*, 31(1), 29-49.



Schott, F. A., & Brandt, P. (2007). Circulation and deep water export of the subpolar North Atlantic during the 1990's. Washington DC American Geophysical Union Geophysical Monograph Series, 173, 91-118.

Sharp, J.D., Pierrot, D., Humphreys, M.P., Epitalon, J.-M., Orr, J.C., Lewis, E.R., Wallace, D.W.R. (2023, Jan. 19). CO2SYSv3 for MATLAB (Version v3.2.1). Zenodo. <http://doi.org/10.5281/zenodo.3950562>

Smeed, D.A., Josey, S.A., Beaulieu, C., Johns, W.E., Moat, B.I., Frajka-Williams, E., Rayner, D., Meinen, C.S., Baringer, M.O., Bryden, H.L., McCarthy, G.D. (2018). The North Atlantic Ocean Is in a State of Reduced Overturning. *Geophysical Research Letters*, 45, 1527–1533. <https://doi.org/10.1002/2017GL076350>

Steinfeldt, R., Rhein, M., Bullister, J.L., Tanhua, T. (2009). Inventory changes in anthropogenic carbon from 1997 – 2003 in the Atlantic Ocean between 20 ° S and 65 ° N, 23, 1–11. <https://doi.org/10.1029/2008GB003311>

Stephens, T. (2021). Ocean Acidification. In: *Research Handbook on Law, Governance and the Planetary Boundaries*. 22, 295–308. <https://doi.org/10.4337/9781789902747.00025>

Stramma, L., Kieke, D., Rhein, M., Schott, F., Yashayaev, I., Koltermann, K.P. (2004). Deep water changes at the western boundary of the subpolar North Atlantic during 1996 to 2001. *Deep Sea Research Part I: Oceanographic Research Papers*, 51, 1033–1056. <https://doi.org/10.1016/J.DSR.2004.04.001>

Sutherland, D. A., and Pickart, R. S. (2008). The East Greenland coastal current: Structure, variability, and forcing. *Progress in Oceanography*, 78(1), 58-77.

Takahashi, T., Olafsson, J., Goddard, J.G., Chipman, D.W., Sutherland, S.C. (1993). Seasonal variation of CO₂ and nutrients in the high-latitude surface oceans: A comparative study. *Global Biogeochemical Cycles*, 7, 843–878. <https://doi.org/10.1029/93GB02263>

Takahashi, T., Sutherland, S.C., Wanninkhof, R., Sweeney, C., Feely, R.A., Chipman, D.W., Hales, B., Friederich, G., Chavez, F., Sabine, C., Watson, A., Bakker, D.C.E., Schuster, U., Metzl, N., Yoshikawa-Inoue, H., Ishii, M., Midorikawa, T., Nojiri, Y., Körtzinger, A., Steinhoff, T., Hoppema, M., Olafsson, J., Arnarson, T.S., Tilbrook, B., Johannessen, T., Olsen, A., Bellerby, R., Wong, C.S., Delille, B., Bates, N.R., de Baar, H.J.W. (2009). Climatological mean and decadal change in surface ocean pCO₂, and net sea-air CO₂ flux over the global oceans. *Deep Sea Research Part II: Topical Studies in Oceanography*, 56, 554–577. <https://doi.org/10.1016/j.dsr2.2008.12.009>

Tanhua, T., Körtzinger, A., Friis, K., Waugh, D.W., Wallace, D.W.R. (2007). An estimate of anthropogenic CO₂ inventory from decadal changes in oceanic carbon content. *Proceedings of the National Academy of Sciences, U.S.A.*, 104, 3037–3042. <https://doi.org/10.1073/pnas.0606574104>



Tesdal, J.E., Abernathy, R.P., Goes, J.I., Gordon, A.L., Haine, T.W.N. (2018). Salinity trends within the upper layers of the subpolar North Atlantic. *Journal of Climate*, 31, 2675–2698. <https://doi.org/10.1175/JCLI-D-17-0532.1>

Thomas, H., Prowe, A.E.F., Lima, I.D., Doney, S.C., Wanninkhof, R., Greatbatch, R.J., Schuster, U., Corbière, A. (2008). Changes in the North Atlantic Oscillation influence CO₂ uptake in the North Atlantic over the past 2 decades. *Global Biogeochemical Cycles*, 22, 1–13. <https://doi.org/10.1029/2007GB003167>

Tjiputra, J.F., Olsen, A., Bopp, L., Lenton, A., Pfeil, B., Roy, T., Segschneider, J., Totterdell, I., Heinze, C. (2014). Long-term surface pCO₂ trends from observations and models. *Tellus, Series B: Chemical and Physical Meteorology*, 66, 1–24. <https://doi.org/10.3402/tellusb.v66.23083>

Touratier, F., Azouzi, L., Goyet, C. (2007). CFC-11, $\Delta^{14}\text{C}$ and 3H tracers as a means to assess anthropogenic CO₂ concentrations in the ocean. *Tellus, Series B: Chemical and Physical Meteorology*, 59, 318–325. <https://doi.org/10.1111/j.1600-0889.2006.00247.x>

Tsuchiya, M., Talley, L.D., McCartney, M.S. (1992). An eastern Atlantic section from Iceland southward across the equator. *Deep Sea Research Part A: Oceanographic Research Papers*, 39, 1885–1917. [https://doi.org/10.1016/0198-0149\(92\)90004-D](https://doi.org/10.1016/0198-0149(92)90004-D)

Urban-Rich, J., Dagg, M., Peterson, J. (2001). Copepod grazing on phytoplankton in the Pacific sector of the Antarctic polar front. *Deep Sea Research Part II: Topical Studies in Oceanography*, 48, 4223–4246. [https://doi.org/10.1016/S0967-0645\(01\)00087-X](https://doi.org/10.1016/S0967-0645(01)00087-X)

Våge, K., Pickart, R.S., Thierry, V., Reverdin, G., Lee, C.M., Petrie, B., Agnew, T.A., Wong, A., Ribergaard, M.H. (2009). Surprising return of deep convection to the subpolar North Atlantic Ocean in winter 2007–2008. *Nature Geoscience*, 2, 67–72. <https://doi.org/10.1038/ngeo382>

Van Aken, H.M., and Becker, G. (1996). Hydrography and through-flow in the north-eastern North Atlantic Ocean: the NANSEN project. *Prog. Oceanogr.* 38, 297–346. [https://doi.org/10.1016/S0079-6611\(97\)00005-0](https://doi.org/10.1016/S0079-6611(97)00005-0)

Van Aken, H. M., and De Boer, C. J. (1995). On the synoptic hydrography of intermediate and deep water masses in the Iceland Basin. *Deep Sea Research Part I: Oceanographic Research Papers*, 42(2), 165–189.

Van Heuven, S., D. Pierrot, J.W.B. Rae, E. Lewis, and D.W.R. Wallace (2011). MATLAB Program Developed for CO₂ System Calculations. ORNL/CDIAC-105b. Carbon Dioxide Information Analysis Center, Oak Ridge National Laboratory, U.S. Department of Energy, Oak Ridge, Tennessee. https://doi.org/10.3334/CDIAC/otg.CO2SYS_MATLAB_v1.1

Vázquez-Rodríguez, M., Padin, X.A., Pardo, P.C., Ríos, A.F., Pérez, F.F. (2012). The subsurface layer reference to calculate preformed alkalinity and air-sea CO₂ disequilibrium in the Atlantic Ocean. *J. Mar. Syst.* 94, 52–63. <https://doi.org/10.1016/j.jmarsys.2011.10.008>



Vázquez-Rodríguez, M., Pérez, F.F., Velo, A., Ríos, A.F., Mercier, H. (2012). Observed acidification trends in North Atlantic water masses. *Biogeosciences* 9, 5217–5230. <https://doi.org/10.5194/bg-9-5217-2012>

Vázquez-Rodríguez, M., Touratier, F., Monaco, C. Lo, Waugh, D.W., Padin, X.A., Bellerby, R.G.J., Goyet, C., Metzl, N., Ríos, A.F., Pérez, F.F. (2009). Anthropogenic carbon distributions in the Atlantic Ocean: Data-based estimates from the Arctic to the Antarctic. *Biogeosciences* 6, 439–451. <https://doi.org/10.5194/BG-6-439-2009>

Wallace, D. W. (2001). Storage and transport of excess CO₂ in the oceans: The JGOFS/WOCE global CO₂ survey. In *International Geophysics* (Vol. 77, pp. 489-L). Academic Press. [https://doi.org/10.1016/S0074-6142\(01\)80136-4](https://doi.org/10.1016/S0074-6142(01)80136-4)

Watson, A.J., Schuster, U., Bakker, D.C.E., Bates, N.R., Corbière, A., González-Davila, M., Friedrich, T., Hauck, J., Heinze, C., Johannessen, T., Körtzinger, A., Metzl, N., Olafsson, J., Olsen, A., Oschlies, A., Antonio Padin, X., Pfeil, B., Magdalena Santana-Casiano, J., Steinhoff, T., Telszewski, M., Rios, A.F., Wallace, D.W.R., Wanninkhof, R. (2009). Tracking the variable North Atlantic sink for atmospheric CO₂. *Science* (80-.). 326, 1391–1393. <https://doi.org/10.1126/science.1177394>

Winkler, L. W. (1888). Die bestimmung des im wasser gelösten sauerstoffes. *Berichte der deutschen chemischen Gesellschaft*, 21(2), 2843-2854.

Xu, X., Hurlburt, H.E., Jr, W.J.S., Zantopp, R., Fischer, J., Hogan, P.J. (2013). On the currents and transports connected with the atlantic meridional overturning circulation in the subpolar North Atlantic. *J. Geophys. Res.* 118, 502–516. <https://doi.org/10.1002/jgrc.20065>

Yashayaev, I. (2007). Hydrographic changes in the Labrador Sea, 1960–2005. *Progress in Oceanography*, 73(3-4), 242-276. <https://doi.org/10.1016/j.pocean.2007.04.015>

Yashayaev, I., Dickson, B. (2008). Transformation and Fate of Overflows in the Northern North Atlantic. In: Dickson, R.R., Meincke, J., Rhines, P. (eds) *Arctic–Subarctic Ocean Fluxes*. Springer, Dordrecht. https://doi.org/10.1007/978-1-4020-6774-7_22

Yashayaev, I., Holliday, N. P., Bersch, M., and van Aken, H. M. (2008). The history of the Labrador Sea Water: Production, spreading, transformation and loss. *Arctic–Subarctic Ocean Fluxes: Defining the Role of the Northern Seas in Climate*, 569-612.

Yashayaev, I., Lazier, J., & Clarke, R. (2003). Temperature and salinity in the central Labrador Sea during the 1990s and in the context of the longer-term change. Retrieved from <https://doi.org/10.17895/ices.pub.19271729>